

SPECTROSCOPY OF ^{15}Be

By

Jesse Daniel Snyder

A DISSERTATION

Submitted to
Michigan State University
in partial fulfillment of the requirements
for the degree of

Physics – Doctor of Philosophy

2014

ABSTRACT
SPECTROSCOPY OF ^{15}Be

By

Jesse Daniel Snyder

The neutron-unbound nucleus ^{15}Be was observed for the first time. It was populated using neutron transfer from a deuterated polyethylene target with a 59 MeV/u ^{14}Be beam. Neutrons were measured in coincidence with outgoing ^{14}Be particles and the reconstructed decay energy spectrum exhibits a resonance at 1.8 ± 0.1 MeV. This corresponds to ^{15}Be being unbound by 0.45 MeV more than ^{16}Be thus significantly hindering the sequential two-neutron decay of ^{16}Be to ^{14}Be through this state. The cross section for neutron pick up was calculated to be 1.1 ± 0.6 mb, and 0.7 ± 0.5 mb from carbon, and deuterium, respectively.

TABLE OF CONTENTS

LIST OF TABLES	v
LIST OF FIGURES	vi
Chapter 1 Introduction	1
1.1 Theory	3
1.2 Previous Work	5
1.3 Populating and Observing ^{15}Be	6
Chapter 2 Experimental Technique and Setup	7
2.1 Invariant Mass Spectroscopy	7
2.2 Beam Production	8
2.3 Experimental Setup	9
2.3.1 Charged Particle Detection	11
2.3.2 Neutron Detection	13
2.4 Electronics and Data Acquisition	14
Chapter 3 Data Analysis	17
3.1 Calibration and Corrections of the Charged Particle Detectors	17
3.1.1 Scintillating Detectors	17
3.1.2 CRDCs	20
3.2 MoNA Calibrations	25
3.2.1 Energy Calibration	25
3.2.2 Timing Calibration	25
3.2.3 Position Calibration	27
3.3 Event Selection	28
3.3.1 Incoming Beam Identification	29
3.3.2 CRDCs Charge Collection Gate	29
3.3.3 Element Identification	30
3.3.4 Isotope Identification	30
3.3.5 Neutron Identification	34
3.4 Invariant Mass Reconstruction	37
3.4.1 The Inverse Map	38
3.4.2 Decay Energy	40
3.4.3 Effect of the Carbon in the Deuterated Polyethylene	41

Chapter 4 Simulations	43
4.1 ST MoNA	43
4.1.1 Initial Parameters	44
4.1.2 Central Track Length Issues	46
4.1.3 Final Checks	48
4.1.4 Geometric Efficiency	50
4.1.5 Resonance Modeling	51
4.2 Geant4	53
4.2.1 Comparison	57
Chapter 5 Results	60
5.1 Resonance Energy	60
5.2 Cross Section	64
5.2.1 Systematic Uncertainty	65
5.2.2 Carbon Target	66
5.2.3 Deuterated Polyethylene Target	67
Chapter 6 Summary and Outlook	71
6.1 Summary	71
6.2 Outlook	72
APPENDIX	74
BIBLIOGRAPHY	77

LIST OF TABLES

Table 1.1	The two neutron configurations with the largest contributions	5
Table 1.2	Spectroscopic Factor (SF) for decaying to the ground and excited state	5
Table 3.1	Thin and thick position correction factors	20
Table 3.2	CRDCs slopes and offsets	24
Table 4.1	The centroid and width of the gaussian distribution used to match the beam profile.	44
Table 5.1	The sources of the systematic uncertainty.	66
Table 5.2	The number of reaction events from different target nuclei for the CD2 target.	70
Table A.1	Optical model potentials parameters used	75
Table A.2	Optical model potentials parameters used	75
Table A.3	Optical model potentials parameters used to model the interaction .	76

LIST OF FIGURES

Figure 1.1	Table of isotopes from hydrogen ($Z = 1$) to oxygen ($Z = 8$). The bound isotopes are shown for each element; the different colors correspond to stable (black), neutron rich (blue), and proton rich (orange) isotope. ^{15}Be and ^{16}Be are both neutron unbound and are indicated by the green boxes.	2
Figure 1.2	Level scheme for neutron rich beryllium isotopes. The solid lines indicate experimentally known levels with the uncertainties being represented by the gray squares, whereas the dashed lines come from NUSHELLX calculations using the WBP Hamiltonian. The arrows show the decay path taken from the population of the $3/2^+$ state as determined from Ref. [17].	3
Figure 2.1	Diagram of the beam production mechanism. The primary beam of ^{18}O is accelerated through the K500 and K1200 until it reaches an energy of 120 MeV/u and strikes a 3196 mg/cm^2 beryllium target. The A1900 fragment separator then selects ^{14}Be fragments from other reaction products.	9
Figure 2.2	Diagram of the experimental vault. It shows the placement of the target, quadrupole triplet, Sweeper magnet, and the detectors. . . .	10
Figure 2.3	Schematic of a Cathode-Readout Drift Chamber (CRDC) (adopted from Ref. [47]).	12
Figure 2.4	Schematic diagram of the timing electronics, logic modules, and DAQ. If there is a valid event in MoNA, the Level 1 logic module sends a signal to the Level 2 logic module which waits for a signal from the thin LU to determine if there is a valid coincidence. If there is a valid coincidence, Level 2 sends a signal to the DAQ to read out all of the electronics. If there is no coincidence in the Level 2 sends out a signal to fast clear the electronics.	15

Figure 3.1	Scintillator charge (energy) spectra. The top two plots are from the thin detector, while the bottom two are from the thick scintillator. The events were gated so that only one isotope was present along with the beam being centered in both detectors. The left plots show the raw energy collected while the right plots show the four PMTs after gain matching. The thin and thick LU, RU, LD, and RD are represented by the color red, black, blue and green, respectively.	18
Figure 3.2	Uncorrected thick left-up energy (left panel) and after the time correction factor has been applied (right panel) plotted against event number. The correction factors were determined for each of the PMT for the thin and thick scintillators.	19
Figure 3.3	ΔE from the thin scintillator (left panel) and corrected ΔE (right panel) is plotted against the horizontal position of the detector. The correction is Z dependent, thus it only straightens the beryllium band.	20
Figure 3.4	CRDC2 raw charge collected values for each pad from a sweep run that illuminated the entire face of the detector.	21
Figure 3.5	CRDC2 calibrated charge collected for each pad from a sweep run that illuminated the entire face of CRDC2. The pedestals have been subtracted, and each pad has been gain matched.	22
Figure 3.6	CRDC1 calibrated charge collected for each pad from a sweep run that illuminated the entire face of CRDC2. The pedestals have been subtracted, and each pad has been gain matched. The color represents the number of counts per bin.	23
Figure 3.7	Example mask run for CRDC2. The best fit (pad number) is plotted vs TAC. The holes are easily identifiable and gates were applied around each one and the centroid a gaussian was used to find the centroid in TAC and best fit (pad number).	23
Figure 3.8	Example mask run for CRDC2 after calibration, CRDC2 x (mm) is plotted vs CRDC2 y (mm).	24
Figure 3.9	Example raw QDC spectra for a single MoNA PMT. The cosmic muon peak can be seen at approximately channel 900, room γ -rays are located at channel 250 and the pedestal is not present since it has been already suppressed. For the linear calibration the pedestal was set to zero and the centroid of the cosmic muon peak was set to 20.5 MeVee.	26

Figure 3.10	Example time difference between the right and left sides of a bar from a cosmic muon run. The edges of the bar are easily identified which allows for a linear calibration to determine the slope and offset. This allows for the determination of where the event took place.	28
Figure 3.11	Flight time for the incoming beam from the A1900 timing scintillator to the target scintillator. The ^{14}Be is centered around 173 ns, with the biggest contaminant coming from lithium which is centered at 161.5 ns.	29
Figure 3.12	CRDC1 padsum plotted against CRDC2 padsum. No gates were applied to this plot. The black line corresponds to the gate used to select for good padsum in CRDC1 and CRDC2.	30
Figure 3.13	Element identification is determined using the time of flight between the target and thin plastic scintillator vs energy loss in the thin plastic scintillator. The elements present are identified in the plot.	31
Figure 3.14	Three dimensional plot of the time of flight from the reaction target to the thin scintillator vs. dispersive angle at the focal plane vs. dispersive position at the focal plane. The plot only contains beryllium isotopes. The bands correspond to different isotopes with the most intense being ^{14}Be	32
Figure 3.15	Projection of Figure 3.14 where the color corresponds to time of flight between the reaction target and the thin scintillator. A band of equal time of flight is fitted to construct a parameter describing the correlations between the dispersive angle and position.	33
Figure 3.16	The parameter x_{tx} versus time of flight between the reaction target and the thin scintillator. Isotopes are identified on the plot, along with where the unreacted beam and reaction products are located for ^{14}Be . The black line corresponds to the gate used to remove contamination of unreacted ^{14}Be . In order to reduce the intensity of the unreacted beam, a gate on beam velocity neutrons in MoNA was applied.	33
Figure 3.17	Energy deposited in MoNA versus the time of flight. The plot only contains events where any beryllium isotope was identified after the Sweeper magnet.	35
Figure 3.18	Neutron time of flight spectrum. The black data points represent the time of flight for all beryllium isotopes whereas the red data points are in coincidence with ^{14}Be fragments.	35

Figure 3.19	Neutron time of flight spectrum. The black data points represent the time of flight for ^{14}Be fragments that were selected using the gate shown in Fig. 3.16. The red data points have an additional gate on deposited energies of more than 3 MeVee.	36
Figure 3.20	The horizontal distribution of neutron events in MoNA from the formation of ^{15}Be by neutron pick-up from the target.	37
Figure 3.21	Reconstructed kinetic energy spectrum which is used to test the inverse map. The data comes from a no target run that was bent into the center of the focal plane box. The reconstructed energy is in complete agreement with the value predicted by LISE++ of 59 MeV/u	39
Figure 3.22	Reconstructed angle spectrum that is used to test the inverse map. The data comes from a no target run that was bent into the center of the focal plane box. The reconstructed angle is centered, confirming that the inverse map is working properly.	40
Figure 3.23	Decay energy spectrum for coincidence ^{14}Be and a neutron is shown by the black data points with their statistical uncertainty. The spectrum was calculated using Eq. 2.6. A resonance can clearly be seen at approximately 2 MeV.	41
Figure 3.24	Decay energy spectrum for deuterated polyethylene and a carbon target. A 300 mg/cm ² carbon target was used for 16 hours, the decay energy for the carbon target (red data points) is compared to the deuterated polyethylene target (black data points). The gates and conditions used to select and calibrate for both targets were the same and the results are statistically identical.	42
Figure 4.1	CRDC position and angle spectrum. Each figure compares data (dot) to ST MoNA simulation (line). The top left, top right, bottom left, and bottom right panel shows the comparison for the CRDC1 horizontal position, horizontal angle, vertical position, and vertical angle, respectively.	45
Figure 4.2	A technical drawing of the beam-line from the target to the focal plane box. The central track length from the target to CRDC1 can be determined using this diagram.	46

Figure 4.3	Experimental and simulation data obtained with the Sweeper magnet's current at 366 A. The blue line represents an ST MoNA simulation, while black points represents experimental data. The left panel reflects a simulated total central track length of 165.4 cm and the right panel uses 172.3 cm.	47
Figure 4.4	Angular distribution of the reaction used in ST MoNA, calculated with FRESCO using the global optical potentials from Refs. [38, 35].	48
Figure 4.5	Comparison of simulation (blue line) to data (black points) for ^{14}Be reaction products located in the focal plane. The parameters are compared are CRDC1 X, Θ_X , Y, and Θ_Y which are located in the upper-left, upper-right, lower-left, and lower-right panel, respectively.	49
Figure 4.6	Comparison of simulation (blue line) to data (black points) for ^{14}Be reaction products located in the focal plane. The parameters are compared are target E, Θ_X , Y, and Θ_Y which are located in the upper-left, upper-right, lower-left, and lower-right panel, respectively.	50
Figure 4.7	Geometric efficiency of the MoNA and Sweeper system. It was calculated for energies between 0 and 5 MeV for a neutron pick-up reaction from deuterium.	51
Figure 4.8	The left panel shows the total carbon-neutron inelastic reaction cross section used in the stock G4Physics class (JENDL-HE). The other six colors show the discrete inelastic reaction cross sections used in the Menate_R code. The right panel shows the hydrogen elastic cross section for G4Physics Class (Green) and Menate_R (Black). Also shown is the carbon elastic cross section for the G4Physics (Red) and Menate_R (Blue). (adopted from Ref. [79])	55
Figure 4.9	Visual representation of the elastic cross sections for iron at different energies from Ref [78]. The cross sections at 30, 50, and 70 MeV were added to Menate_R, and then extrapolated to the energy of the neutron.	56
Figure 4.10	Experimental data (Black) from Ref. [77] is compared to the G4Physics (Red) and Menate_R (Blue) model. The left panel shows the multiplicity and right panel shows the energy deposited. In the left panel the multiplicity distributions were normalized so that multiplicity = 1 events matched. The right panel was normalized for total number of events. (adopted from Ref. [79])	58

Figure 4.11	Comparison between the stock G4Physics (Red) and Menate_R (Blue) models of multiplicity distribution for interactions within MoNA where γ rays are produced from inelastic reactions with carbon. (adopted from Ref. [79])	58
Figure 5.1	^{15}Be decay energy spectrum. The data are shown by the black data points with statistical error bars. The best fit to the data (solid black line) is a sum of an $l = 2$ resonance (green short-dashed line) and background contributions approximated by $l = 0$ (red long-dashed line) and $l > 0$ (blue dotted line) components.	61
Figure 5.2	Partial experimental level scheme for neutron rich beryllium isotopes. The height of the gray boxes represents the uncertainties of the states. The data for the excited state in ^{14}Be is from [26], the lower limit for the $3/2^+$ is from [17], the ^{15}Be $5/2^+$ state is from the present work and the two-neutron separation energy for ^{16}Be is from [13].	63
Figure 5.3	RBS simulations using 3.4 MeV protons impinging upon a carbon (red line) and a CH_2 (black line) target are compared to data from RBS analysis, also using 3.4 MeV protons. The carbon data (red points) and deuterated polyethylene data (black points) were normalized to the simulated carbon target. There is good agreement between the simulated deuterated polyethylene target and the data, which indicates that the ratio of carbon to hydrogen is 1:2.	68
Figure 5.4	RBS data for five different locations on the deuterated polyethylene target, impinged with 3.4 MeV protons. Each data set was normalized so the total number of incoming protons were the same. The strength of the peak between channel 30 and 70 is indicative of the percentage of hydrogen in the target is deuterium.	69

Chapter 1

Introduction

One of the fundamental questions of modern nuclear physics has been aimed at better understanding the strong nuclear force. This has been supported by the development of the liquid drop model [1, 2], and the nuclear shell model [3, 4, 5]. The nuclear shell model, in particular, was developed in 1949 and used to explain magic numbers. While the nuclear shell model works well near stability, research has shown that as you approach the drip-line the model starts to break down. The development of in-flight radioactive ion beams in the 1980s [6] has allowed exploration up to and beyond the low- Z neutron drip-line. Implementation of this isotope formation technique has allowed observations of novel effects such as neutron halo nuclei [7], neutron radioactivity [8], and new magic numbers observed away from stability [9, 10].

Probing the effects of the strong nuclear force requires protons and neutrons to be combined in different combinations to determine their resulting properties. One- and two-proton removal reactions as well as light-particle transfer reactions have been used to populate unbound nuclei from neutron unbound hydrogen (up to ${}^7\text{H}$ [11]) to fluorine (${}^{28}\text{F}$ [12]) isotopes. Of recent interest are nuclei which decay by the emission of two neutrons; a particular case is the ground state of ${}^{16}\text{Be}$, which was observed to decay by the emission of two strongly correlated neutrons. This decay at 1.35 ± 0.10 MeV has been interpreted as a dineutron emission [13, 14, 15]. The analysis of two-proton radioactivity has shown that diproton emission

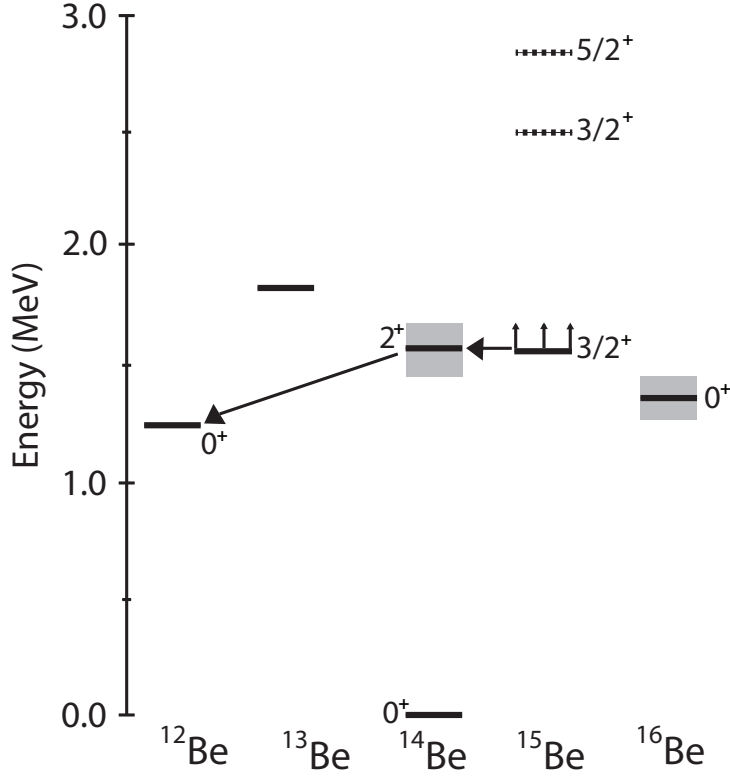


Figure 1.2: Level scheme for neutron rich beryllium isotopes. The solid lines indicate experimentally known levels with the uncertainties being represented by the gray squares, whereas the dashed lines come from NUSHELLX calculations using the WBP Hamiltonian. The arrows show the decay path taken from the population of the $3/2^+$ state as determined from Ref. [17].

1.1 Theory

The level structure of ^{15}Be is unknown and theoretical predictions differ. While early shell model calculations predicted a $5/2^+$ ground state with an excited $3/2^+$ state at 70 keV [18] more recent calculations with NUSHELLX [19] in the s - p - sd - pf model space and the WBP Hamiltonian [20] resulted in a $3/2^+$ ground state and $5/2^+$ excited state at 300 keV. NUSHELLX calculates that the $3/2^+$ ground state of ^{15}Be will be unbound by 2.5 MeV. The predicted level structure of ^{15}Be is shown in Fig 1.2 by the dotted lines.

The previous attempt [17] to populate states of ^{15}Be with the two-proton removal reaction from ^{17}C set a lower limit for the $3/2^+$ state of 1.54 MeV as indicated in the figure. From the

non-observation of neutrons in coincidence with ^{14}Be it was suggested that the $3/2^+$ state probably decays to the first (unbound) excited state in ^{14}Be . Kondo et al. [21] recently showed that this 2^+ state in ^{14}Be decays directly to the ground state of ^{12}Be with the emission of two neutrons as the sequential decay via the ground state of ^{13}Be is energetically not allowed. The black arrows in Figure 1.2 show this decay path of the $3/2^+$ state in ^{15}Be .

The $^{17}\text{C}(-2\text{p})^{15}\text{Be}$ reaction was not expected to populate the $5/2^+$ state in ^{15}Be which still could possibly be the ground state located at an energy where it could serve as an intermediate state for the sequential decay of ^{16}Be . An alternative way to populate the $5/2^+$ state in ^{15}Be is the (d,p) transfer reaction in inverse kinematics with a secondary ^{14}Be beam. This type of transfer reaction has been previously used to study neutron unbound states in ^9He [22, 23, 24] and ^{27}Ne [25] at GANIL but this was the first time it was attempted at NSCL with the MoNA setup.

The 0^+ ground state of ^{14}Be is dominated by the $(0s)^2(0p)^6(0d_{5/2})^2$ and $(0s)^2(0p)^6(0s_{1/2})^2$ configurations as shown in Table 1.1. The table also lists the two dominant neutron configurations of the $3/2^+$ and $5/2^+$ states in ^{15}Be . It is apparent that a neutron transferred to ^{14}Be into the $d_{5/2}$ orbital has a large overlap with the $5/2^+$ state. In contrast, in this simplified picture it is not possible to transfer a neutron to the $d_{5/2}$ or the $s_{1/2}$ orbital and couple it to the 0^+ state to form a $3/2^+$ state.

The possible decay paths of these two states back to ^{14}Be are determined by the spectroscopic factors which are listed in Table 1.2. The spectroscopic factors consider all neutron configurations in each state and not just the dominant configurations shown in Table 1.1. The $3/2^+$ state is predicted to have a much weaker overlap with the ground state in ^{14}Be , but a much stronger overlap with the first excited state in ^{14}Be . This indicates that if the $3/2^+$ state of ^{15}Be is populated and if it is unbound by more than the energy for the first

Table 1.1: The two neutron configurations with the largest contributions to the ground state in ^{14}Be and the two lowest states in ^{15}Be

Isotope	J^π	$0s_{1/2}$	$0p_{3/2}$	$0p_{1/2}$	$0d_{5/2}$	$1s_{1/2}$	$0d_{3/2}$	Contribution
^{14}Be	0^+	2	4	2	2	0	0	46%
^{14}Be	0^+	2	4	2	0	2	0	33%
^{15}Be	$3/2^+$	2	4	2	3	0	0	42%
^{15}Be	$3/2^+$	2	4	2	2	1	0	37%
^{15}Be	$5/2^+$	2	4	2	3	0	0	47%
^{15}Be	$5/2^+$	2	4	2	1	2	0	25%

excited state, 1.54 MeV [26], it will predominantly decay through the first excited state of ^{14}Be which will subsequently decay to ^{12}Be . The predicted decay path is shown in the level scheme of neutron rich beryllium isotopes in Fig. 1.2. The $5/2^+$ state is predicted to have a strong overlap with the ground state of ^{14}Be and will be studied in this thesis.

Table 1.2: Spectroscopic Factor (SF) for decaying to the ground and excited state of ^{14}Be , ℓ corresponds to the angular momentum of the decayed neutron.

State in ^{15}Be	ℓ	0^+ SF	2^+ SF
$3/2^+$	0	0	0.084
$3/2^+$	2	0.043	1.28
$5/2^+$	0	0	0.15
$5/2^+$	2	0.66	0.096

1.2 Previous Work

Previously, little was known experimentally about ^{15}Be . It has never explicitly been found to be unbound. The heavier isotone ^{16}B is unbound [27, 28]; it can thus be deduced that ^{15}Be also is unbound with respect to neutron emission. The previously mentioned two-proton removal reaction was expected to populate predominantly the $3/2^+$ state because it had

been shown that the spin and parity of the ground state of ^{17}C is $3/2^+$ [30, 31, 32]. This suggests that when two-protons are removed from ^{17}C the remaining neutrons should have the same configuration. Thus ^{17}C will have a strong overlap with the $3/2^+$ state and not the $5/2^+$ state of ^{15}Be . From the non-observation of any ^{14}Be fragments, it was concluded that any populated states of ^{15}Be must be located above the unbound first excited state of ^{14}Be , 1.55 MeV [26], and thus decay by the emission of three sequential neutrons into ^{12}Be . The non-observation also confirms the theoretical predictions that the $3/2^+$ state has a strong spectroscopic overlap with the first excited state in ^{14}Be .

1.3 Populating and Observing ^{15}Be

As mentioned earlier, a different method for populating the ^{15}Be states other than the two-proton removal from ^{17}C had to be found. The reaction selected in the present work was neutron pick-up from the target by the secondary beam of ^{14}Be forming ^{15}Be . The neutron will transfer to the ^{14}Be core and is expected to strongly populate single particle states such as the $5/2^+$ state of ^{15}Be .

To predict the rate that the $5/2^+$ state would be populated in this reaction, the coupled channel reaction code FRESKO [33] was employed. The example input file for a transfer reaction on page 446 from Ref. [34] was modified to account for the different initial and final isotopes, along with changing the optical potentials. FRESKO requires optical model potentials between ^{14}Be and ^2H , ^{14}Be and ^1H , and ^{15}Be and ^1H . The parameters used are listed in Appendix . The calculation was done using a single proton global optical potential [35] and several different deuterium global optical potentials [36, 37, 38]; which resulted in a cross section of 1–2 mb for the $5/2^+$ state.

Chapter 2

Experimental Technique and Setup

2.1 Invariant Mass Spectroscopy

The neutron-unbound state in ^{15}Be decays through neutron emission, a process which happens on an incredibly short time scale ($\sim 10^{-21}$ s). The decay products are the residual charged fragment and the neutron. The decay energy of the state in ^{15}Be is measured using a technique called invariant mass spectroscopy which is derived from the conservation of the relativistic four-momentum, \mathbf{P} :

$$\mathbf{P} = (E, \vec{p}). \quad (2.1)$$

E is the total energy, and \vec{p} the three-vector momentum. Conservation of \mathbf{P} is expressed as:

$$\mathbf{P}_i = \mathbf{P}_f + \mathbf{P}_n \quad (2.2)$$

where the subscripts i , f , and n refer to the initial nucleus, residual nucleus, and the emitted neutron, respectively. Squaring both sides of Eq. 2.2 yields:

$$\mathbf{P}_i^2 = (\mathbf{P}_f + \mathbf{P}_n)^2 \equiv M^2 \quad (2.3)$$

where M is defined as the invariant mass of the system. Equation 2.3 can be expressed as:

$$M^2 = (E_f + E_n)^2 - \|\vec{p}_f + \vec{p}_n\|^2 \quad (2.4)$$

By expanding and taking the square root of Eq. 2.4, the expression for M becomes:

$$M = \sqrt{m_f^2 + m_n^2 + 2(E_f E_n - p_f p_n \cos\theta)}. \quad (2.5)$$

where θ is the angle between the fragment and neutron. By subtracting the masses of the decay products from Eq. 2.5, an expression for the decay energy can be found:

$$E_{decay} = \sqrt{m_f^2 + m_n^2 + 2(E_f E_n - p_f p_n \cos\theta)} - m_f - m_n. \quad (2.6)$$

In order to make a measurement of the decay energy, as expressed in Eq. 2.6, it is necessary to measure the energy and angle of the residual fragment and the neutron as they leave the target. The method for calculating these variables is explained in Section 3.4.

2.2 Beam Production

States in ^{15}Be were populated utilizing a secondary ^{14}Be beam where a neutron was picked up from either the carbon or deuterium in the deuterated polyethylene target. ^{14}Be is radioactive with a half life of ~ 4 ms [39], and was produced with the method of fast fragmentation [40].

A diagram of the beam production mechanism is shown in Fig. 2.1. A stable beam of ^{18}O is first accelerated to 120 MeV/u in the NSCL coupled K500 and K1200 cyclotrons [41]. It then impinges on a beryllium target with a thickness of 3196 mg/cm². The beam undergoes reactions within the target, producing a large variety of isotopes. These reaction



Figure 2.1: Diagram of the beam production mechanism. The primary beam of ^{18}O is accelerated through the K500 and K1200 until it reaches an energy of 120 MeV/u and strikes a 3196 mg/cm^2 beryllium target. The A1900 fragment separator then selects ^{14}Be fragments from other reaction products.

products pass through the A1900 fragment separator [42] which selects ^{14}Be based on the magnetic rigidity, $B\rho = p/q$. A 1050 mg/cm^2 achromatic aluminum wedge is located after the second dipole to disperse reaction products and improve separation. Slits are located at the intermediate focal plane, which allows for selecting different momentum acceptances for the A1900. The momentum acceptance was initially set to 0.5%. To increase the beam rate, the momentum acceptance was changed to 2% for the final 80% of production. The ^{14}Be secondary beam was focused beyond the target, in order to increase the acceptance, with an energy of 59 MeV/u.

2.3 Experimental Setup

A diagram of the experimental setup is shown in Fig. 2.2. At the end of the A1900 fragment separator, the beam passes through the first (not shown) of two plastic scintillators which

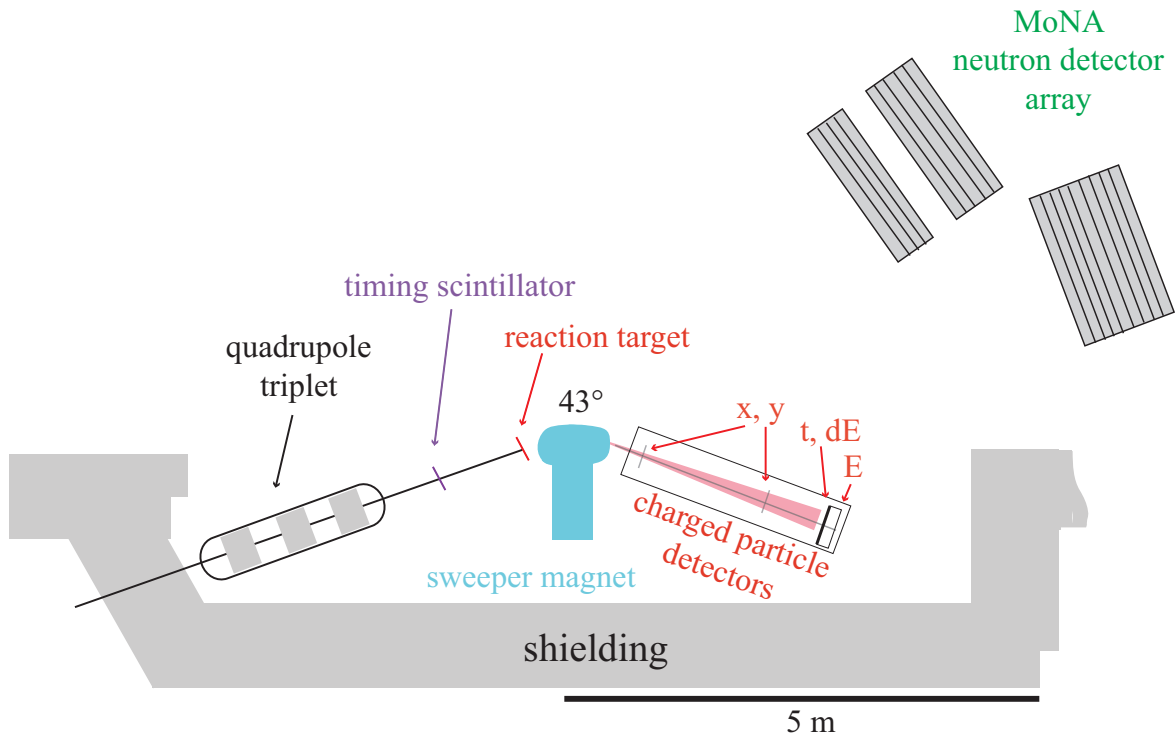


Figure 2.2: Diagram of the experimental vault. It shows the placement of the target, quadrupole triplet, Sweeper magnet, and the detectors.

provide a measurement of the time of flight. Before the second timing scintillator the beam passes through a quadrupole triplet, which focuses the beam onto the reaction target. The primary target was made of deuterated polyethylene with a thickness of 435 mg/cm^2 which was used for 85% of the experiment. The secondary target which was used for 15% of the experiment was a 308 mg/cm^2 carbon target.

After the beam underwent reactions in the deuterated polyethylene target, it is necessary to measure both the residual charged fragments and the neutrons. The neutrons continue traveling at nearly beam velocity and are recorded using the Modular Neutron Array (MoNA)

[43, 44] which was split into two sections, centered at -6° and 23° . Charged fragments also continue at nearly beam velocity, but are deflected away from zero degrees by a dipole called the Sweeper magnet [45] with a bending angle of 43° , a radius of one meter, and a maximum rigidity of 4 Tm. It has a large vertical gap of 14 cm, which allows the neutrons to travel to MoNA uninhibited. The magnet was set to 3.55 Tm to optimize transmission for ^{14}Be reaction products. After the magnet the charged particles pass through two position sensitive Cathode Readout Drift Chambers (CRDC) and a thin plastic scintillator before stopping in a thick plastic scintillator.

2.3.1 Charged Particle Detection

As previously mentioned, the incoming time of flight is measured by two scintillators which allows for removal of contaminants with off-line analysis. The first detector is located at the focal plane of the A1900 fragment separator the second detector is located 104 cm upstream from the reaction target, resulting in a total flight path of 10.44 m. When a charged particle passes through a plastic scintillator, it creates electron-hole pairs, which recombine creating photons. The photons are then collected in a photo-multiplier tube (PMT) that is optically coupled to the plastic. The PMT converts the photons into an electrical signal and then amplifies it so that it can be recorded. The detection process happens on a fast timescale, allowing for a detection resolution of under one nanosecond. The A1900 scintillator is 1008 μm thick, whereas the target scintillator is 254 μm thick. Each scintillator is made of BC-404 (H_{10}C_9) [46] and is coupled to a single PMT which then feeds the signal into a constant fraction discriminator (CFD).

To determine the vector of the charged particle after the sweeper two position sensitive Cathode-Readout Drift Chamber (CRDC) are used. A schematic of a CRDC is shown in

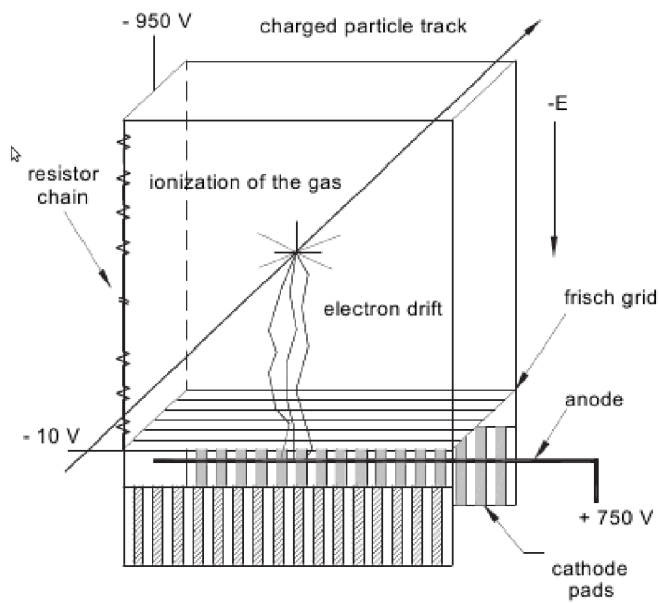


Figure 2.3: Schematic of a Cathode-Readout Drift Chamber (CRDC) (adopted from Ref. [47]).

Fig. 2.3. The CRDCs have an area of $30 \times 30 \text{ cm}^2$ and are filled with 80% CF_4 and 20% iso-butane at a pressure of 50 Torr. When charged particles pass through the gas it ionizes some of the molecules, releasing electrons. The electrons are subject to a -850 V drift voltage, causing them to drift upwards to an anode wire which collects the charge. The anode wire is held at +950 V. Located near the anode wire are 128 aluminum pads, spaced 2.54 mm apart from each other. The charge collected on the anode wire induces a charge on these pads.

The dispersive position is determined using the distribution of the charge collected on the aluminum pads. The charge collected on each pad is plotted as a function of pad number and fitted with a gaussian to determine the centroid. The centroid is then converted from pad space into physical dimensions using a linear transformation. The vertical position is determined by the time difference between the anode signal and the master trigger.

Downstream of the two CRDCs are two additional plastic scintillators, also made of BC-404, covering a $40 \times 40 \text{ cm}$ area. Due to their large area, they both use four PMTs coupled near the corners labeled as thin_{LU} , thin_{LD} , thin_{RU} , and thin_{RD} , respectively. The upstream scintillator is 0.5 cm thick and the downstream scintillator is 15 cm thick. The thin scintillator is used for energy loss and timing, whereas the thick scintillator stops the charged fragment and gives an indication of the total energy.

2.3.2 Neutron Detection

MoNA consists of 144 bars of plastic scintillator, each measuring $200 \text{ cm} \times 10 \text{ cm} \times 10 \text{ cm}$. Each bar is made of BC-408, which has a hydrogen to carbon ratio of 1.104 [46]. Both ends of a bar are coupled through a light guide to a PMT. The modular nature of MoNA allows for multiple configurations. In this experiment MoNA was split with nine walls located 650 cm

from the target at -6° with 8 bars in each wall. The rest of the bars located 470 cm from the target at 23° were split into two groups, with the first four walls separated by 60 cm from the last five walls. Likewise each wall consists of eight bars. The split configuration was chosen to achieve the largest possible acceptance for the expected large decay energy of ^{15}Be .

Neutrons, due to their lack of electrical charge, cannot directly excite the electrons of the scintillating material of MoNA. When neutrons passing through MoNA hit a proton, that proton is then dislodged from the lattice in the bar producing scintillation light. Then, the light travels along the bar until it is collected by both PMTs. The light is collected and amplified by each PMT and then converted into an electrical signal. The anode signal is fed into a CFD, which then sends a pulse into a time-to-digital converter (TDC). The time difference between the target scintillator and the TDC signal is used to determine the neutron's time of flight from the target to MoNA.

2.4 Electronics and Data Acquisition

The electronics and data acquisition (DAQ) of the setup have been described extensively in Ref. [47, 48]. In this section, the timing components along with the interplay between the Sweeper and MoNA setup will be discussed. A diagram of the electronics and DAQ for running MoNA and the Sweeper setup is shown in Fig. 2.4.

The trigger logic is handled by programmable Xilinx Logic Modules (XLMs), which are separated into “Level 1” and “Level 2”. Level 1 determines if a good event has occurred in MoNA and then passes that information onto Level 2. A good event occurs when there is at least one bar that has a valid time signal in both CFDs. The Level 2 then waits for a

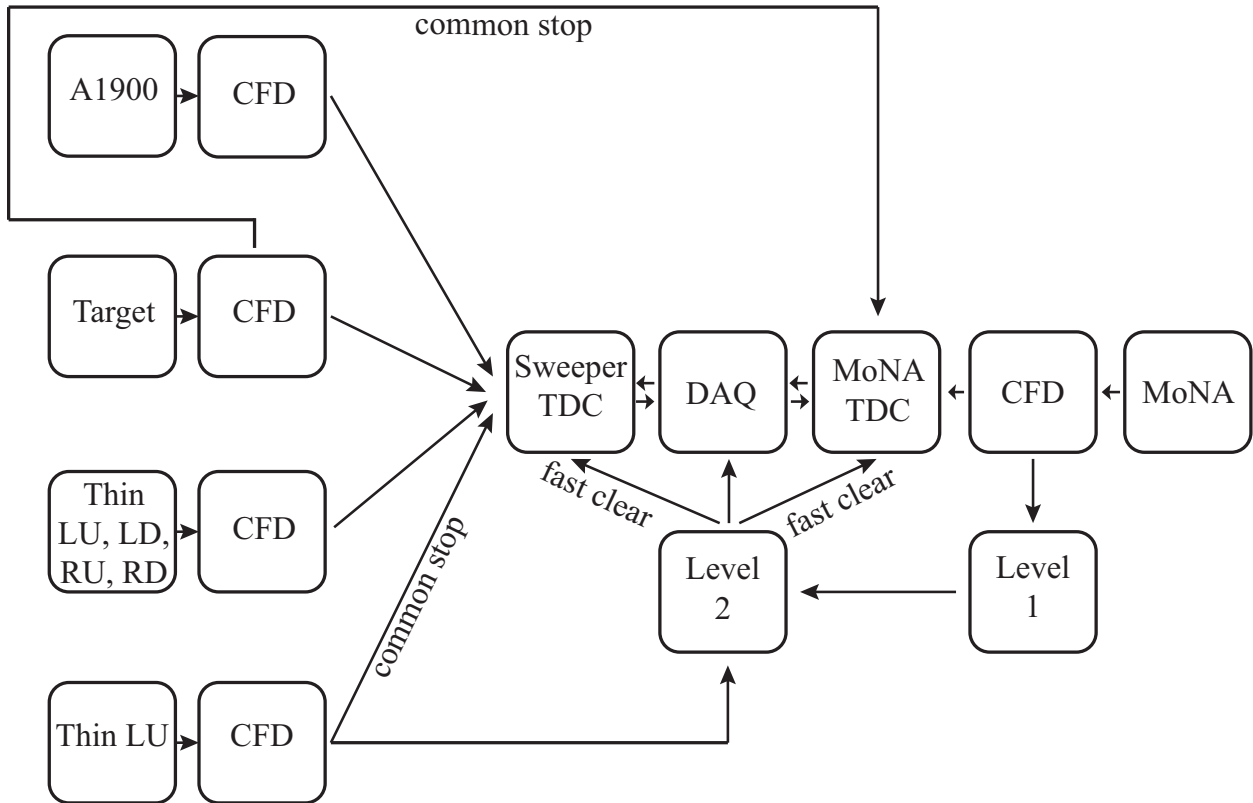


Figure 2.4: Schematic diagram of the timing electronics, logic modules, and DAQ. If there is a valid event in MoNA, the Level 1 logic module sends a signal to the Level 2 logic module which waits for a signal from the thin LU to determine if there is a valid coincidence. If there is a valid coincidence, Level 2 sends a signal to the DAQ to read out all of the electronics. If there is no coincidence in the Level 2 sends out a signal to fast clear the electronics.

trigger signal from the Sweeper side, with the trigger for the Sweeper side coming from the thin_{LU} . Once the Level 2 has a coincidence from both MoNA and the Sweeper it sends the signal for the DAQ to read out the data in the electronics.

The signal from thin_{LU} is split into two signals. The first signal is the Sweeper trigger that goes to the Level 2. The second signal goes to the Sweeper TDC and provides the stop signal for all the TDCs. The start signal for the TDCs comes from all the other timing scintillators in the Sweeper setup. The scintillator at the target is also split. The first signal goes to the Sweeper TDC as previously discussed. The second signal is sent to MoNA and is used as the stop signal for MoNA's TDCs.

Chapter 3

Data Analysis

3.1 Calibration and Corrections of the Charged Particle Detectors

3.1.1 Scintillating Detectors

The relative time between the beam passing through the A1900, target, and thin scintillators is used to select for the incoming ^{14}Be , and isotope separation after the sweeper magnet. Element selection is performed using the thin and thick scintillator which record the ΔE and E_{total} , respectively. Each of the timing detectors along the beam-line and in the focal plane box record the time of interaction relative to the master trigger (t_{thinLU}). The time of interaction for each PMT is calculated by:

$$t^{cal} = (t^{raw} - t_{thinLU}^{raw}) * 0.1 \frac{ns}{ch} + t_{offset} \quad (3.1)$$

where t_{raw} is the timing signal from the A1900, the target, or the four PMTs in the thin scintillator.

The thin scintillator uses four PMTs, unlike the A1900 and target scintillators which only use a single PMT each. The time from each PMT is averaged to determine the proper time. A beam down center run is used to find the offset of each PMT with respect to the

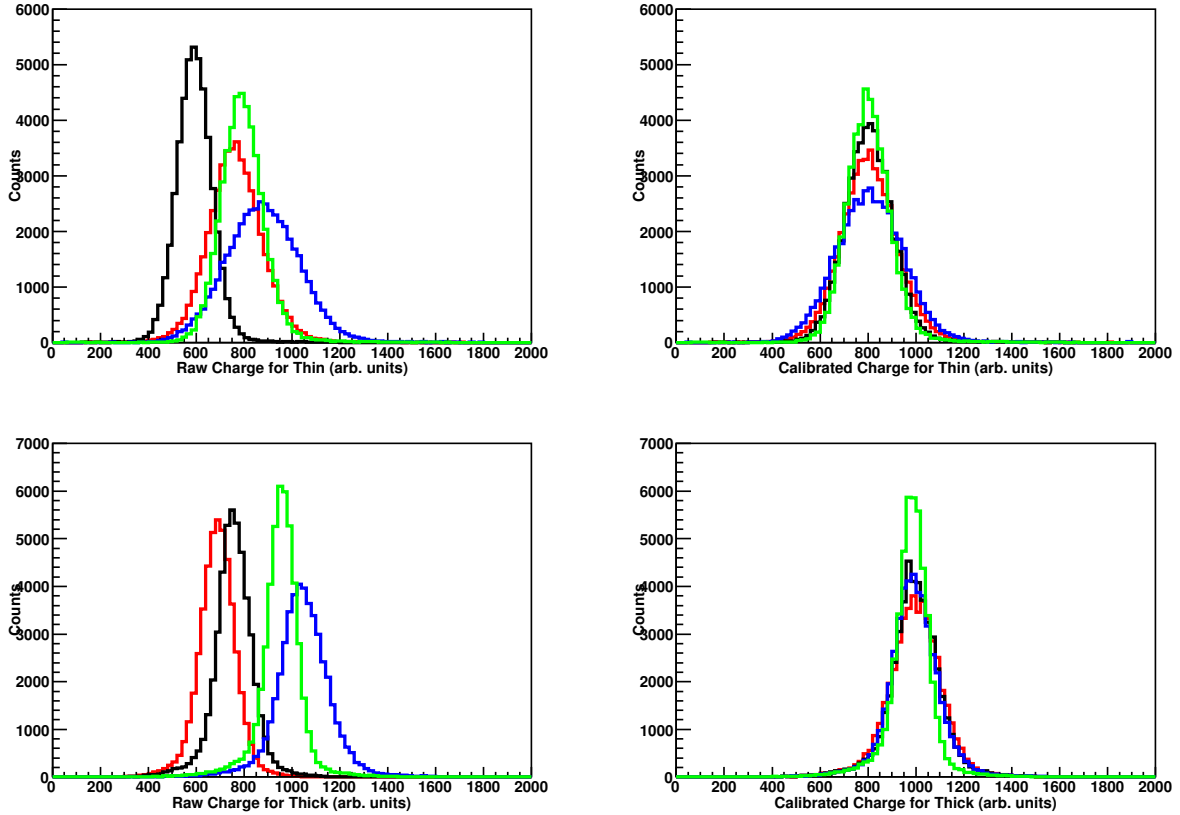


Figure 3.1: Scintillator charge (energy) spectra. The top two plots are from the thin detector, while the bottom two are from the thick scintillator. The events were gated so that only one isotope was present along with the beam being centered in both detectors. The left plots show the raw energy collected while the right plots show the four PMTs after gain matching. The thin and thick LU, RU, LD, and RD are represented by the color red, black, blue and green, respectively.

reference PMT (thin_{LU}).

The calibration of the energy for the thin and thick plastic scintillators requires gain matching and position correction. Due to instability in the PMTs it was necessary to also correct for drifts in time. The first step is to gain match which requires that the light attenuation be the same for each of the PMTs. To meet this requirement it was necessary to select events where the interaction was in the center of the scintillators. The signal of each PMT was fit with a gaussian, and a correction factor determined to move the centroids to channel 800 and 1000 for the thin and thick scintillator, respectively. The left side of

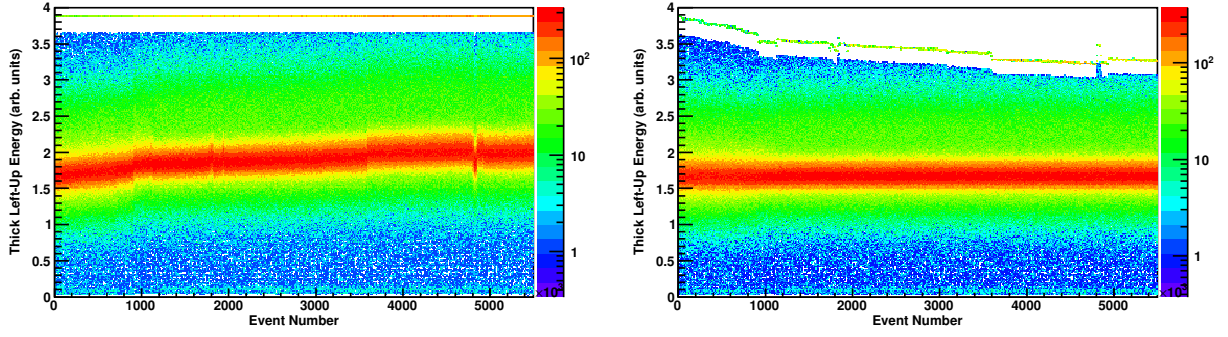


Figure 3.2: Uncorrected thick left-up energy (left panel) and after the time correction factor has been applied (right panel) plotted against event number. The correction factors were determined for each of the PMT for the thin and thick scintillators.

Fig. 3.1 shows the raw energy for the four PMTs in the thin (top) and the thick (bottom) scintillator, while the right side shows the gain matched energy.

To correct for the drifts in time for each PMT, the data was broken into 10,000 blocks. The centroid of each block was found by fitting with a gaussian and a correction factor determined. The correction factor was then applied to the energy collected by each PMT on an event by event basis. Figure 3.2 shows the uncorrected thick right-up (left panel) and once it has been corrected for drifts in time (right panel). The correction factors varied by 3–10% and 8–20% for the thin and thick scintillators, respectively.

After each PMT has been gain matched and corrected for drifts in time, the deposited energy is calculated using:

$$E_{dep} = \frac{\sqrt{e_{top}^2 + e_{bottom}^2}}{2} \quad (3.2)$$

where e_{top}^2 and e_{bottom}^2 are the averaged energy from the top and bottom two PMTs for the thick and thin scintillators. The scintillator energy is left in arbitrary units, since they are only used to select for different reaction products.

The final step is to remove any correlations between horizontal and vertical position of the

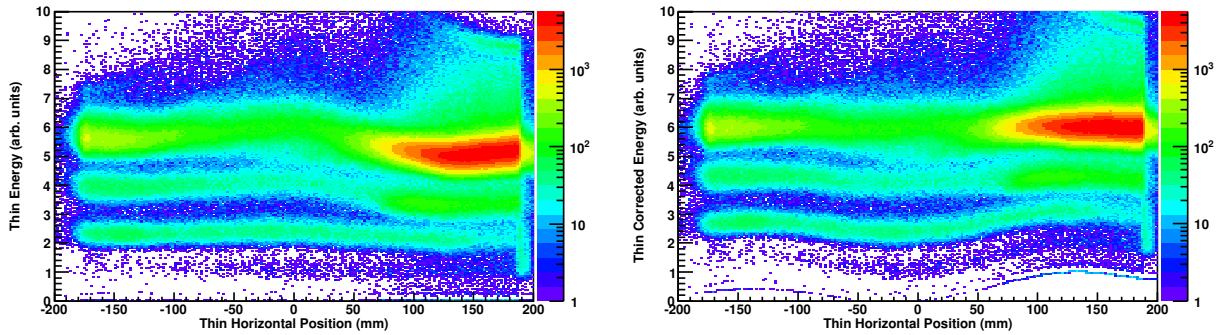


Figure 3.3: ΔE from the thin scintillator (left panel) and corrected ΔE (right panel) is plotted against the horizontal position of the detector. The correction is Z dependent, thus it only straightens the beryllium band.

interaction and the calculated energy. A third order polynomial was used and the correction factors are located in Table 3.1.

Table 3.1: Thin and thick position correction factors

	1st order	2nd order	3rd order
Thin Horizontal	1.42	0.0377	$-3.68 \cdot 10^{-5}$
Thin Vertical	1.005	-0.0199	$7.52 \cdot 10^{-5}$
Thick Horizontal	-2.53	$-7.63 \cdot 10^{-4}$	$-3.24 \cdot 10^{-5}$
Thick Vertical	-1.173	0.0	0.0

Figure 3.3 shows the uncorrected (left panel) and the corrected (right panel) thin energy plotted against the horizontal position. The corrections used were Z dependent and were only optimized for beryllium.

3.1.2 CRDCs

As explained in Section 2.3.1 the CRDC's horizontal and vertical position are determined from the charge distribution on the pads and the time difference from the start (master trigger) and the stop (CRDC anode wire) signals, respectively. Each pad of the CRDCs is sampled eight times and the resulting charge is summed to determine the total charge

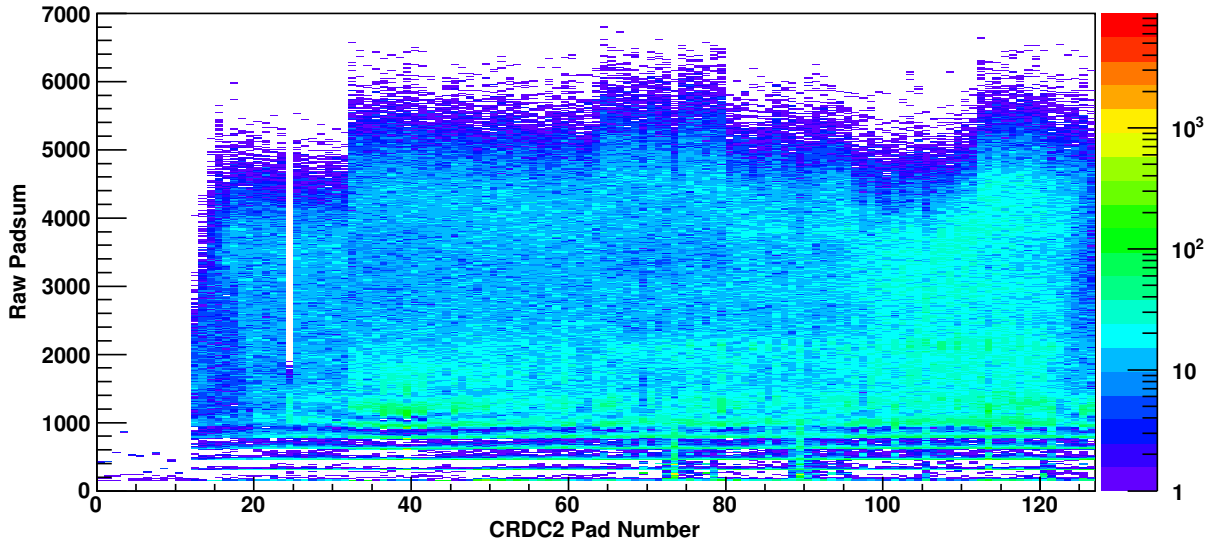


Figure 3.4: CRDC2 raw charge collected values for each pad from a sweep run that illuminated the entire face of the detector.

collected during each event. To calibrate the horizontal position it is necessary to determine the pedestals. For this purpose data was recorded where no signals were present in the CRDCs; the pedestals were then calculated by fitting the total charge with a gaussian.

Once the pedestals are subtracted each pad needs to be gain matched. The strength of the magnetic field of the Sweeper magnet was varied, illuminating the entire CRDC2. The charge collected for each pad, when it collected the most charge, was fitted with a gaussian and a correction factor was determined to move the peak to the average value for all pads. The correction factors needed were within 20% of the average value. Fig 3.4 is a plot of the raw charge collected for each pad of CRDC2, whereas Fig 3.5 shows the calibrated charged collected for each pad.

Certain pads display charge collection characteristics that are not indicative of actual events. These pads are typically noisy pads and need to be removed from analysis. The charge collected for each pad was examined and the noisy pads were removed from future

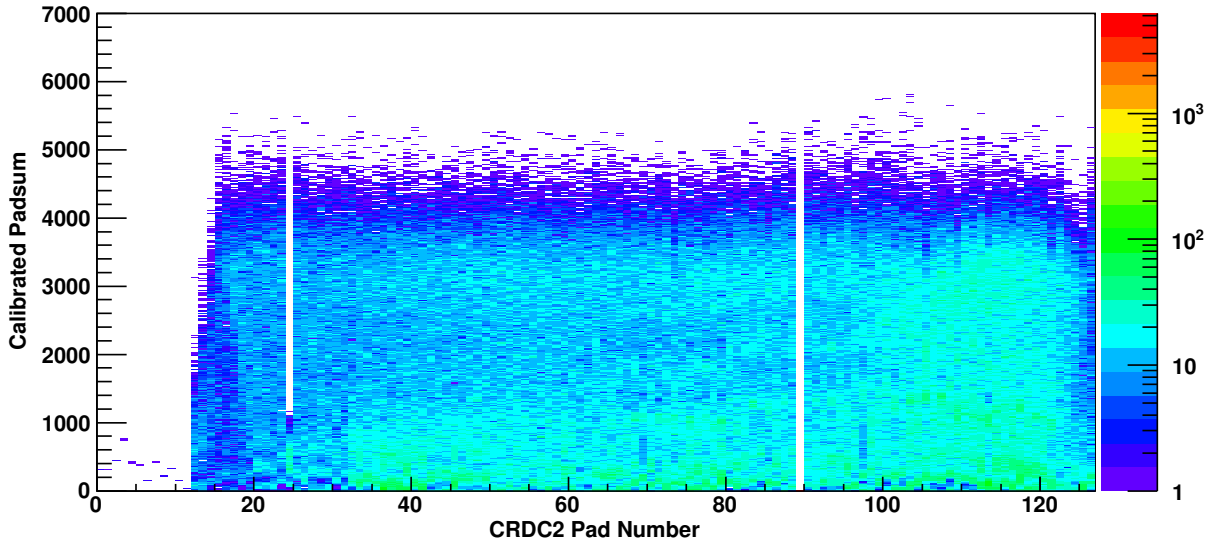


Figure 3.5: CRDC2 calibrated charge collected for each pad from a sweep run that illuminated the entire face of CRDC2. The pedestals have been subtracted, and each pad has been gain matched.

analysis. CRDC1 pads 96 - 110 had to be removed from analysis. Fortunately these pads were not typically illuminated. CRDC2 had two bad pads, 24 and 89.

To determine which pad the interaction was closest to, a fit of the plot of charge collected by pad number was fit with a gaussian. The gaussian can still accurately find the centroid of the interaction even if it took place near a bad pad. The vertical interaction is determined by using a TAC which records the time difference between the start (thin left-up) and the stop (CRDC anode wire). Fig 3.7 shows a plot of TAC vs best pad fit for a mask run of CRDC2.

Now that the pedestals have been suppressed and each pad has been gain matched, it is necessary to determine the slope and offsets required to convert the pad space and tac data and into physical units of position. A tungsten mask with holes drilled into known locations was inserted in front of each CRDC, shadowing the detector. The incoming beam was then defocused and swept across the focal plane to illuminate as many holes as possible. The

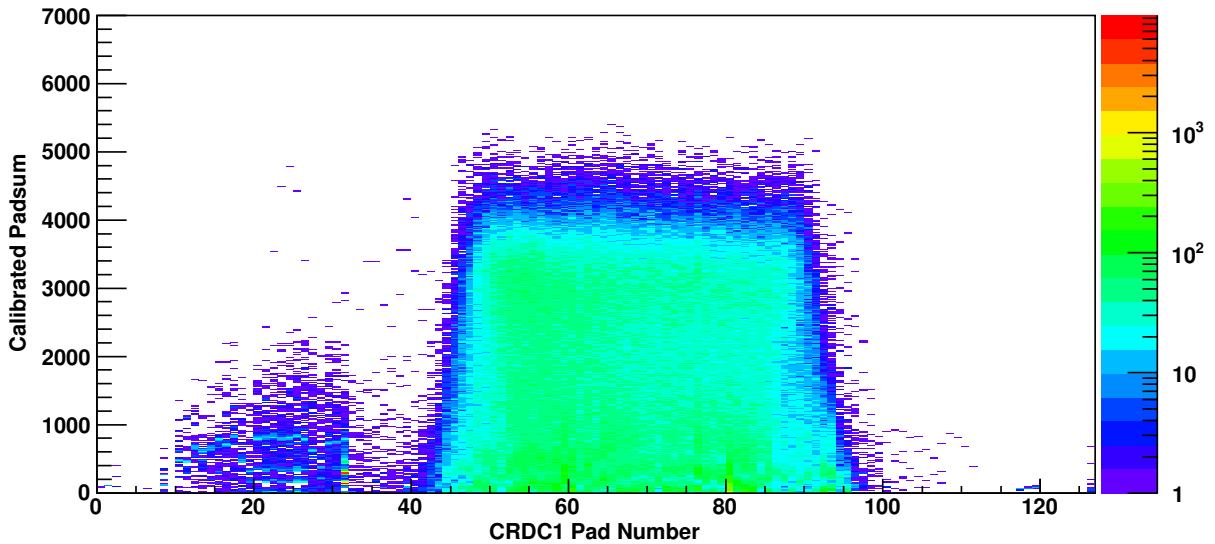


Figure 3.6: CRDC1 calibrated charge collected for each pad from a sweep run that illuminated the entire face of CRDC2. The pedestals have been subtracted, and each pad has been gain matched. The color represents the number of counts per bin.

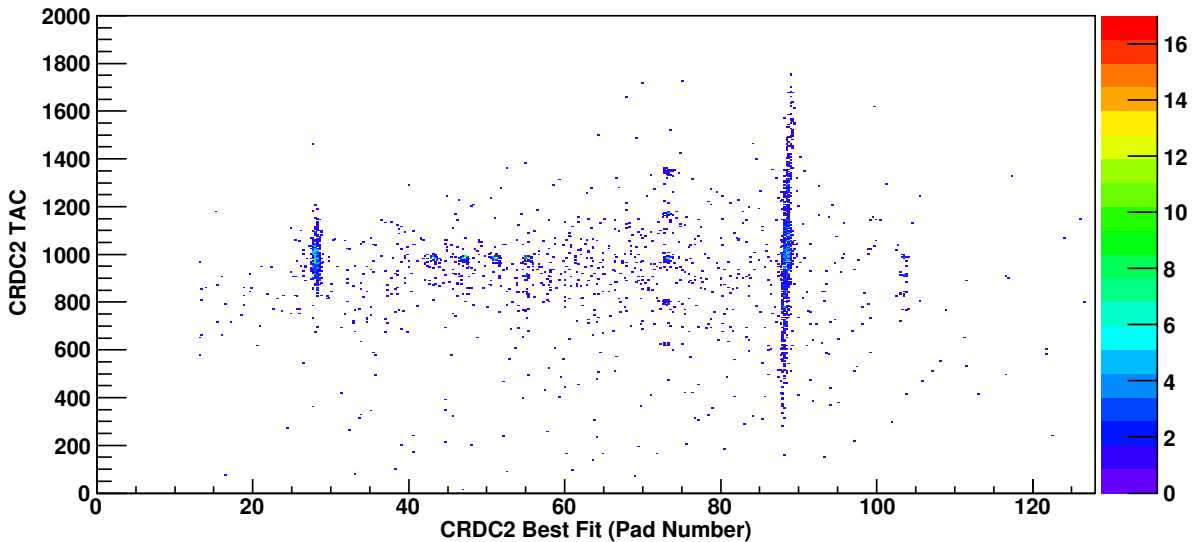


Figure 3.7: Example mask run for CRDC2. The best fit (pad number) is plotted vs TAC. The holes are easily identifiable and gates were applied around each one and the centroid a gaussian was used to find the centroid in TAC and best fit (pad number).

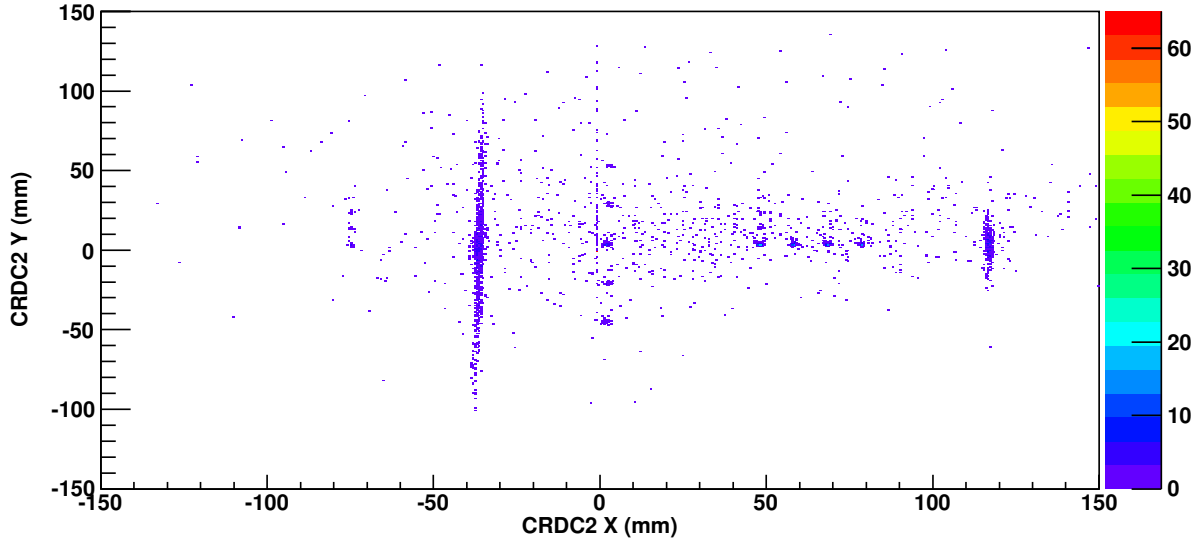


Figure 3.8: Example mask run for CRDC2 after calibration, CRDC2 x (mm) is plotted vs CRDC2 y (mm).

conversion from pad space to physical units is a simple linear transformation using the pad spacing of 2.54 mm/pad. To determine the slope and offset for the vertical axis, along with the horizontal axis offset, the centroid for the holes in pad space vs tac were converted into physical units. A sample mask run is shown in Fig. 3.7.

During the experiment the masks were driven in for each CRDC at three separate occasions. The results for both detectors were consistent with the average values from the three runs, and were then used for the entire experimental run. The values determined for the vertical slope and offset, along with the horizontal offset, are shown in Table 3.2. Fig 3.8 is an example plot demonstrating that the linear transformation from tac and pad space into physical space has been accomplished.

Table 3.2: CRDCs slopes and offsets

Device	Y slope (mm/ch)	Y offset (mm)	X offset (mm)
CRDC1	-0.135	137.74	-175.21
CRDC2	-0.135	125.78	185.14

3.2 MoNA Calibrations

3.2.1 Energy Calibration

Due to differences in light transmission through the plastic bars and amplification of the PMTs, each PMT must be individually gain matched. This is done with cosmic muons which deposit on average 20.5 MeVee of energy into each MoNA bar. Online gain matching is used to move the cosmic muon peak to approximately the same channel. Figure 3.9 shows an example histogram where the cosmic muon peak is at approximately channel 900.

Once the bias voltage for each PMT has been adjusted to line up the muon peaks, a software routine is applied to the signal from each PMT to acquire the slopes and offsets necessary to convert from channels to units of MeVee. The automated routine finds the pedestal value and the muon peak is fit with a gaussian. The centroid is used to determine the exact channel of the muon peak. A linear slope and offset is then derived to place the pedestal at zero and the muon peak at 20.5 MeVee [49].

3.2.2 Timing Calibration

To determine the slopes for the TDCs in MoNA, a time calibrator that sends a signal every 40 ns was plugged into the modules. The average of both PMTs was taken to derive the time of interaction. From this point it is necessary to determine two offsets. The first is the individual offset for each bar relative to a reference bar. This will make the whole array's timing self-consistent. The second offset is a global offset that ties the array together with the reaction target.

Cosmic muons are used to determine the individual offset. The muons are produced in the upper atmosphere from cosmic rays and are traveling at nearly the speed of light,

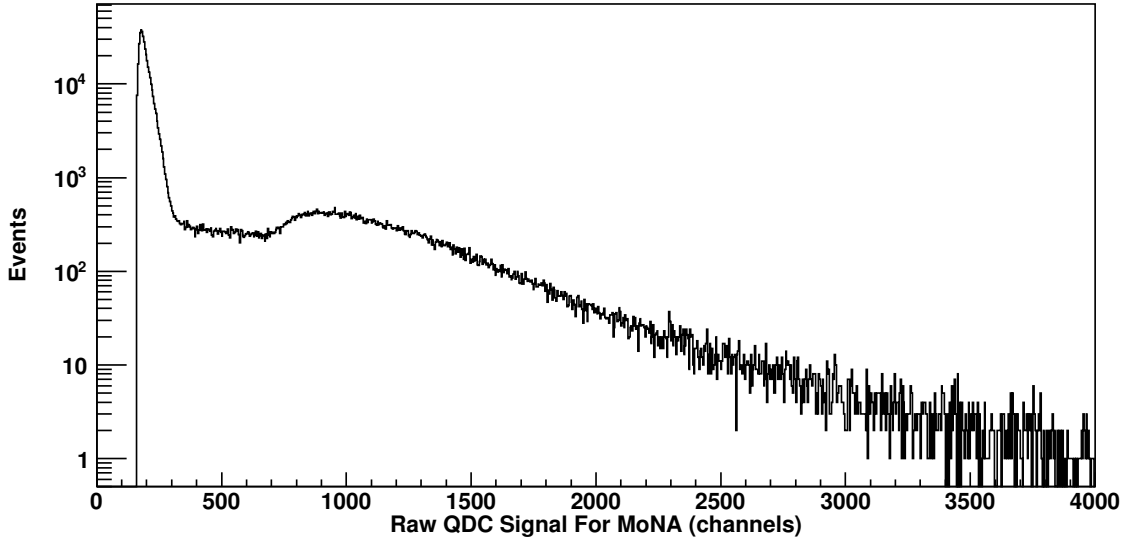


Figure 3.9: Example raw QDC spectra for a single MoNA PMT. The cosmic muon peak can be seen at approximately channel 900, room γ -rays are located at channel 250 and the pedestal is not present since it has been already suppressed. For the linear calibration the pedestal was set to zero and the centroid of the cosmic muon peak was set to 20.5 MeVee.

29.9 cm/ns [50]. The individual offset is determined in a two step process. First, each wall is tied together using muons that are traveling mostly vertical. To accomplish this a gate that requires all 8 bars in a wall have events is used. To determine the expected time, t_μ , between the top bar and the bar in question Eq. 3.3 is used, where n is the number of bars between the two bars, 10.3 cm is the average distance between the center of two adjacent bars and 29.9 cm/ns is the average velocity of a muon at the surface of the earth. Appropriate offsets are then determined by comparing the expected time from Eq. 3.3 and the measured time difference.

$$t_\mu = \frac{n \cdot 10.3 \text{ cm}}{29.9 \text{ cm/ns}} \quad (3.3)$$

To determine the offset for each wall, it is necessary to look at diagonal muon tracks. Each wall was tied to the top bar in the front wall by diagonal muon tracks. This allowed

for offsets for each wall to be determined. MoNA was split into two separate arrays, with each array being separated by a large enough distance that it was impractical to find muons that hit both arrays. Thus it was necessary to give each array a different global offset.

To determine the offset for each array, prompt γ -rays made in the target were selected. The expected time of flight was then determined using:

$$ToF_{\gamma} = \frac{d}{29.98 \text{ cm/ns}} \quad (3.4)$$

where d is the distance from the target to where the interaction took place in cm.

The global offsets for both arrays were determined by comparing the expected time of flight of the γ -rays with the measured time of flight. For low energy γ -rays there is a walk despite using constant fraction discriminators (CFD). The walk was characterized in Ref. [51]; above 2.5 MeVee the walk was almost non-existent. To compensate for the walk a gate of 3 MeVee was applied when determining the global offset for both arrays. To remove contamination of unreacted beam arriving in coincidence with room γ -rays, a gate of 3 MeVee was applied to the data set. This removed the necessity of correcting for the low energy walk of the CFDs.

3.2.3 Position Calibration

To determine the energy and momentum of the neutron it is necessary to know where the neutron interacted within MoNA. A laser sighting system was used to determine where the front face of both arrays were located relative to the target. The next step was to determine where along the bar the interaction took place. The time difference between the right and left PMT is directly related to the location in the bar where the interaction took place. In Fig.

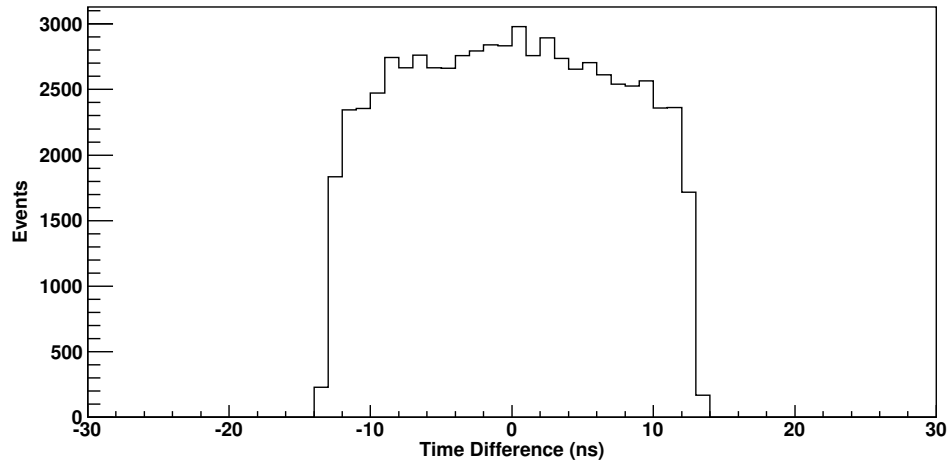


Figure 3.10: Example time difference between the right and left sides of a bar from a cosmic muon run. The edges of the bar are easily identified which allows for a linear calibration to determine the slope and offset. This allows for the determination of where the event took place.

3.10, the time difference between the right and left signal is plotted. From this histogram, a linear calibration is used to determine the slope and offset necessary to determine where along the bar the interaction took place.

3.3 Event Selection

During the experiment, for every event of interest, it was necessary to record approximately 10,000 events. The events of interest are when the ^{14}Be beam picks up a neutron from the deuterated polyethylene target forming ^{15}Be , which then decays back down to the ground state of ^{14}Be . If instead of decaying to the ground state it decays into the first excited state of ^{14}Be at 1.54 MeV [26], it will cascade down into ^{12}Be and is of no interest in this analysis. This section will detail the event selection gates used to select for the reaction process of interest.

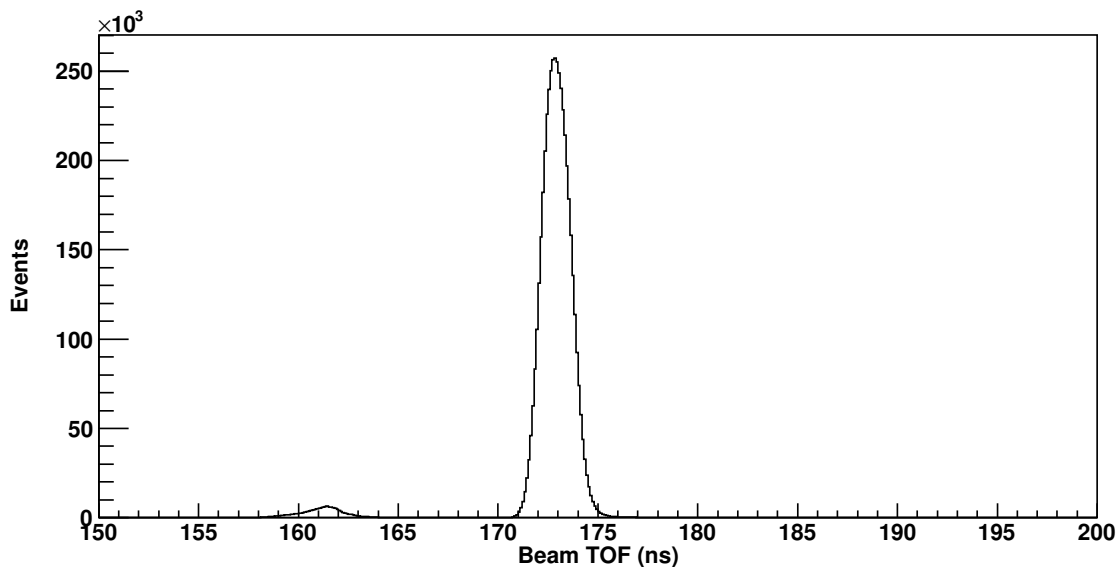


Figure 3.11: Flight time for the incoming beam from the A1900 timing scintillator to the target scintillator. The ^{14}Be is centered around 173 ns, with the biggest contaminant coming from lithium which is centered at 161.5 ns.

3.3.1 Incoming Beam Identification

Figure 3.11 shows the flight time between the scintillator in the focal plane of the A1900 fragment separator and the target scintillator. This parameter was used to select for incoming ^{14}Be . The primary contaminant was lithium which arrived at ~ 10 ns before ^{14}Be . These two components are easily separated by the difference in their time of flight between the a1900 scintillator and the target scintillator.

3.3.2 CRDCs Charge Collection Gate

To separate the isotopes along with reconstructing the fragment's energy and momentum at the target, it is necessary to have accurate horizontal position information in both CRDCs. To accomplish this it is necessary for both CRDCs to have significant charge collected; which allows for an accurate measurement of the position of the interaction.

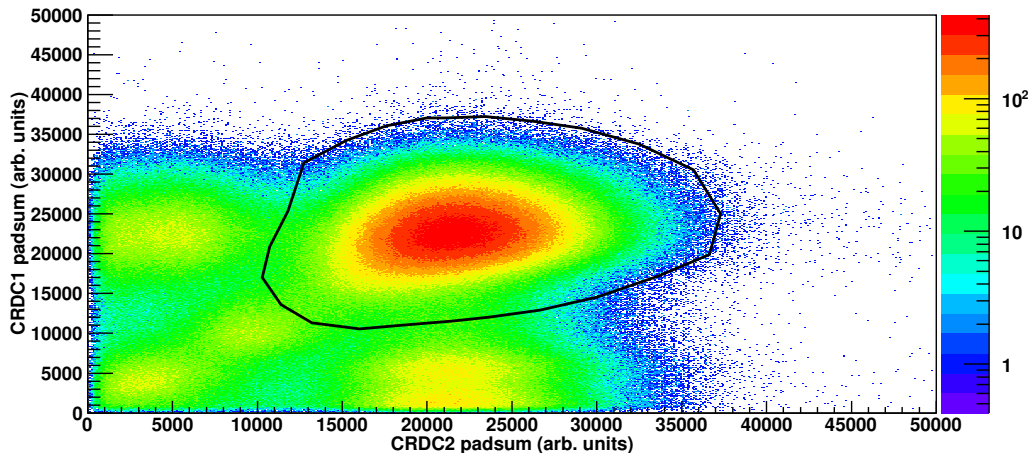


Figure 3.12: CRDC1 padsum plotted against CRDC2 padsum. No gates were applied to this plot. The black line corresponds to the gate used to select for good padsum in CRDC1 and CRDC2.

Figure 3.12 shows a plot of CRDC2 padsum vs. CRDC1 padsum. The black line shows the gate applied to select for good charge collection in both CRDCs. The CRDCs charge collection is dependent on the charge of the incoming beam and in this experiment they were also used as a poor element gate along with primarily being used to require a good horizontal interaction point.

3.3.3 Element Identification

Element separation was achieved by plotting the corrected dE from the thin detector against the time of flight from the target to the thin detector as shown in Figure 3.13. Beryllium, lithium, and helium are cleanly identified.

3.3.4 Isotope Identification

The Sweeper magnet, with its large total momentum acceptance of 12.6% along with its inability to focus the fragments in position, makes it difficult to achieve isotope separation.

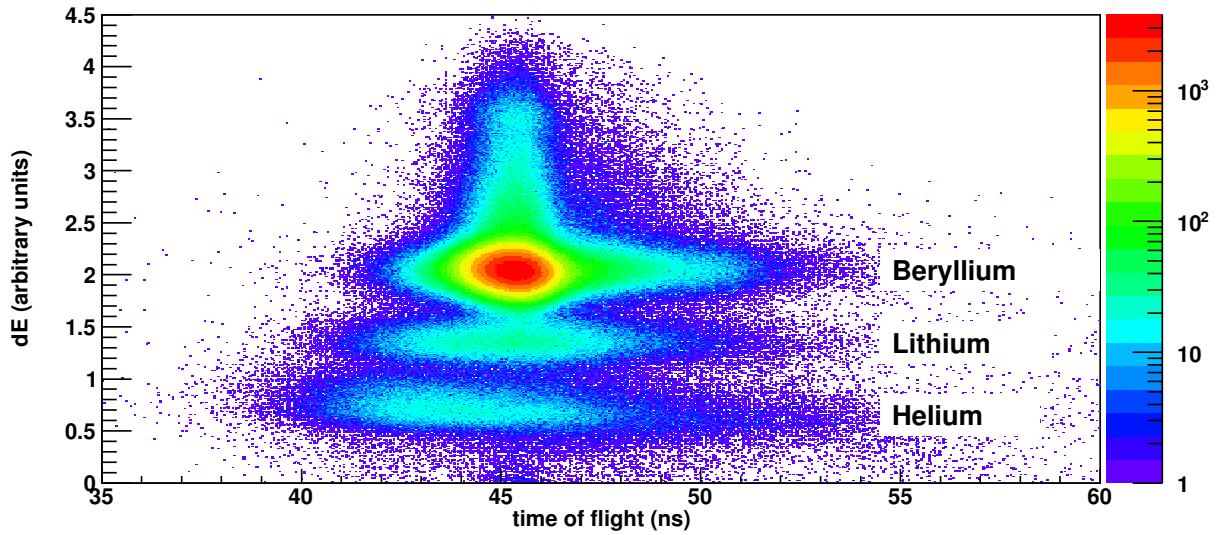


Figure 3.13: Element identification is determined using the time of flight between the target and thin plastic scintillator vs energy loss in the thin plastic scintillator. The elements present are identified in the plot.

To achieve isotope separation it is necessary to understand the correlations between the dispersive position, dispersive angle, and the time of flight between the reaction target and the thin scintillator.

The first step is to make a plot of the time of flight between the reaction target and the thin scintillator vs. dispersive angle vs. dispersive position, at the focal plane of the Sweeper magnet. The focal plane is located 0.657 m before CRDC1. This is shown in Figure 3.14; the plot requires that both CRDCs have good position information along with that only beryllium is present. The isotope bands can be identified, but it is impractical to make a three dimensional gate.

Once isotope bands can be seen in the three dimensional plot it is necessary to project it onto the dispersive angle and position plane, as shown in Fig. 3.15, where the color corresponds to the time of flight between the reaction target and thin scintillator. In order to understand the correlations between the dispersive angle and position a fit along a band

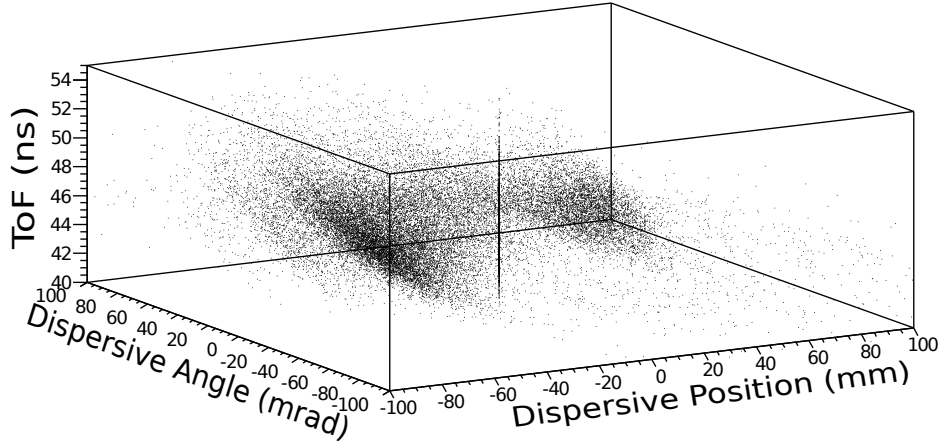


Figure 3.14: Three dimensional plot of the time of flight from the reaction target to the thin scintillator vs. dispersive angle at the focal plane vs. dispersive position at the focal plane. The plot only contains beryllium isotopes. The bands correspond to different isotopes with the most intense being ^{14}Be .

of equal time of flight, as shown in Figure 3.15, is necessary. The fit gives the correlation between focus position and angle to be:

$$x_{tx} = \theta_{x, focus} - 0.911x_{focus} - 0.00585x_{focus}^2 - 6.27 \cdot 10^{-5}x_{focus}^3 \quad (3.5)$$

The parameter x_{tx} when plotted against of time of flight between the reaction target and the thin scintillator allows for isotope separation as shown in Figure 3.16. Each isotope is cleanly identified, along with the gap where ^{13}Be should be if it was not neutron unbound. The unreacted beam is identified in Fig. 3.16; it was necessary to apply a cut eliminating the unreacted beam to reduce the contamination from unreacted ^{14}Be . This cut is shown by the black line.

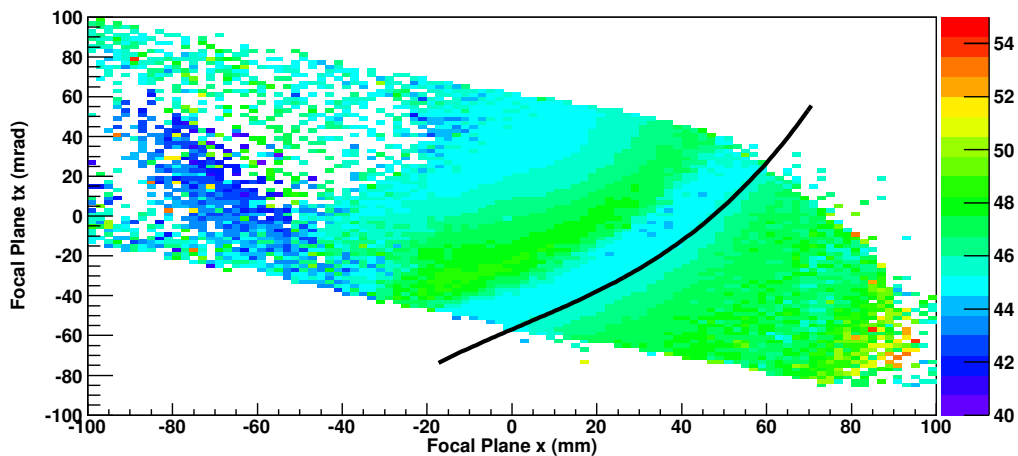


Figure 3.15: Projection of Figure 3.14 where the color corresponds to time of flight between the reaction target and the thin scintillator. A band of equal time of flight is fitted to construct a parameter describing the correlations between the dispersive angle and position.

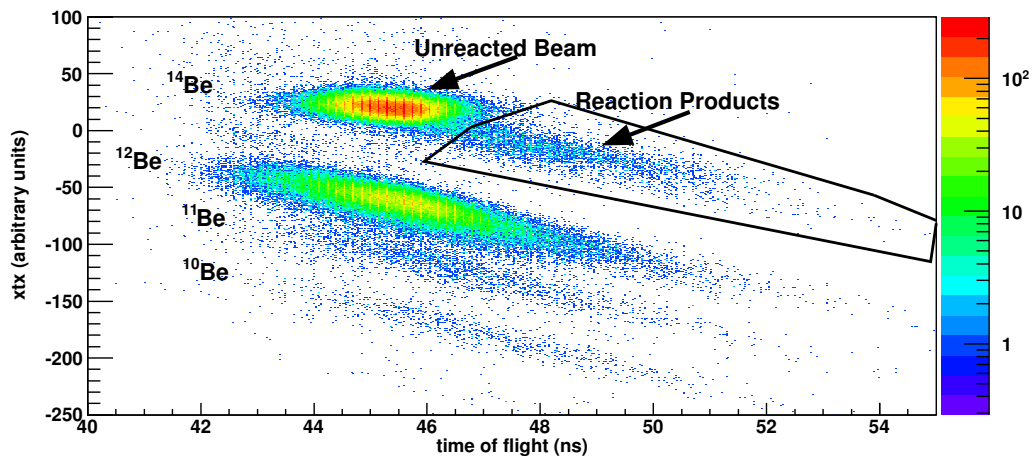


Figure 3.16: The parameter xtx versus time of flight between the reaction target and the thin scintillator. Isotopes are identified on the plot, along with where the unreacted beam and reaction products are located for ^{14}Be . The black line corresponds to the gate used to remove contamination of unreacted ^{14}Be . In order to reduce the intensity of the unreacted beam, a gate on beam velocity neutrons in MoNA was applied.

3.3.5 Neutron Identification

MoNA determines the time, location, and energy deposited for each interaction within one of its bars. In previous MoNA experiments which predominantly utilized one- or two-proton removal reactions, the time-of-flight spectra were clean and contained only beam velocity neutrons from the decay of populated states. However, in the present case of a neutron pick-up reaction where the decay product is the same as the incident beam, a significant background from random coincidences is observed.

Figure 3.17 shows the time of flight versus the energy deposited in MoNA. This figure was gated on identified beryllium isotopes. The large triangular area between 50 and 80 ns and reaching up to 80 MeVee corresponds to beam velocity neutrons from the decay of neutron-unbound beryllium fragments. No γ -rays originating from the target, which would appear at 21 ns, are visible. Instead, a strong peak at 60 ns depositing less than 5 MeVee was identified as γ -rays originating from inside the focal plane box. In addition two time-independent broad background distributions can be observed. The band that deposits less than 3 MeVee comes from room background γ -rays, whereas the band that deposits 20 to 30 MeVee is due to cosmic muons.

The projection of Fig. 3.17 onto the time-of-flight axis is shown in Fig. 3.18 as the black data points. It is dominated by beam velocity neutrons around 70 ns. The shoulder at shorter times is due to the γ -rays from inside the focal plane box. When an additional gate on ^{14}Be fragments only is applied (red data points), the majority of the beam velocity neutrons disappear indicating that they originate predominantly from ^{12}Be . Now the γ -rays from the focal plane box are the largest peak with an additional enhancement at longer times (~ 90 ns) become visible. These events could be due to neutrons emitted from the target or

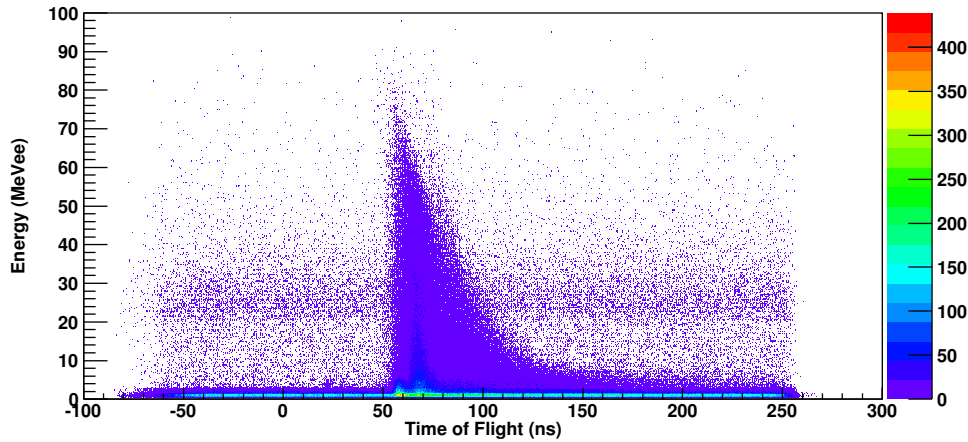


Figure 3.17: Energy deposited in MoNA versus the time of flight. The plot only contains events where any beryllium isotope was identified after the Sweeper magnet.

from the beam hitting inside the focal plane box.

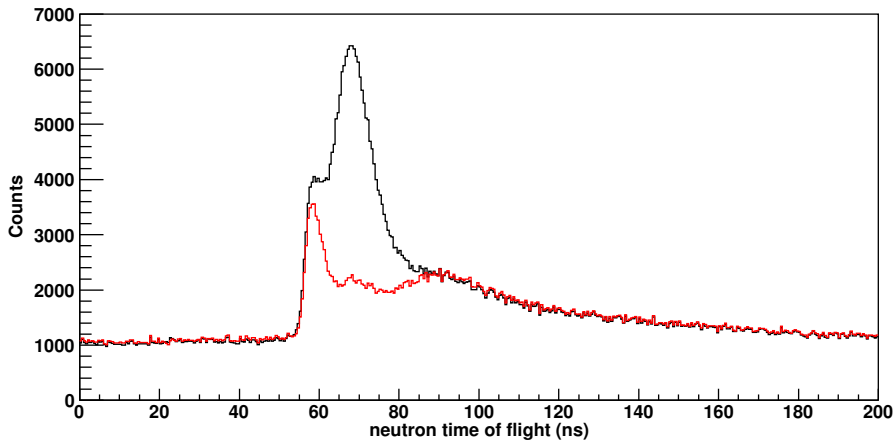


Figure 3.18: Neutron time of flight spectrum. The black data points represent the time of flight for all beryllium isotopes whereas the red data points are in coincidence with ^{14}Be fragments.

The background can be further reduced by applying the gate on ^{14}Be reaction products from Figure 3.16. This gate has been applied for the black data points in Figure 3.19 and eliminates the focal plane γ -rays. Remaining contributions from room background γ -rays are removed by applying another gate on deposited energies in MoNA of more than 3 MeVee. The resulting time-of-flight spectrum is shown by the red data points in Figure 3.19. The

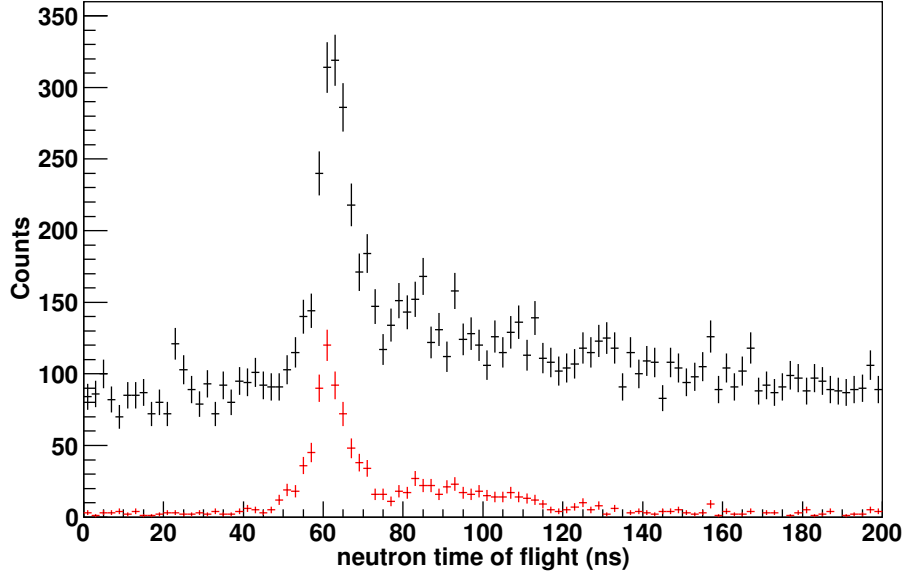


Figure 3.19: Neutron time of flight spectrum. The black data points represent the time of flight for ^{14}Be fragments that were selected using the gate shown in Fig. 3.16. The red data points have an additional gate on deposited energies of more than 3 MeVee.

spectrum has three distinct features: prompt neutrons from the $d(^{14}\text{Be},^{15}\text{Be})p$ reaction, slower neutrons most likely produced in the target or focal plane box, and a negligible constant background of events from cosmic muons spread out evenly throughout the time of flight. For the calculation of the decay energy spectrum only events between 45 and 75 ns were selected. The same cut is also applied in all simulations.

The distribution of the beam velocity neutron in the horizontal directions across MoNA is shown in Fig. 3.20. The distribution peaks around 0° and indicates neutrons emitted from beam velocity fragments. In addition, the acceptance at larger distances is limited by the vertical gap of the Sweeper magnet. The gap between 50 and 100 cm corresponds to the gap between the two parts of MoNA centered at -6° and 23° .

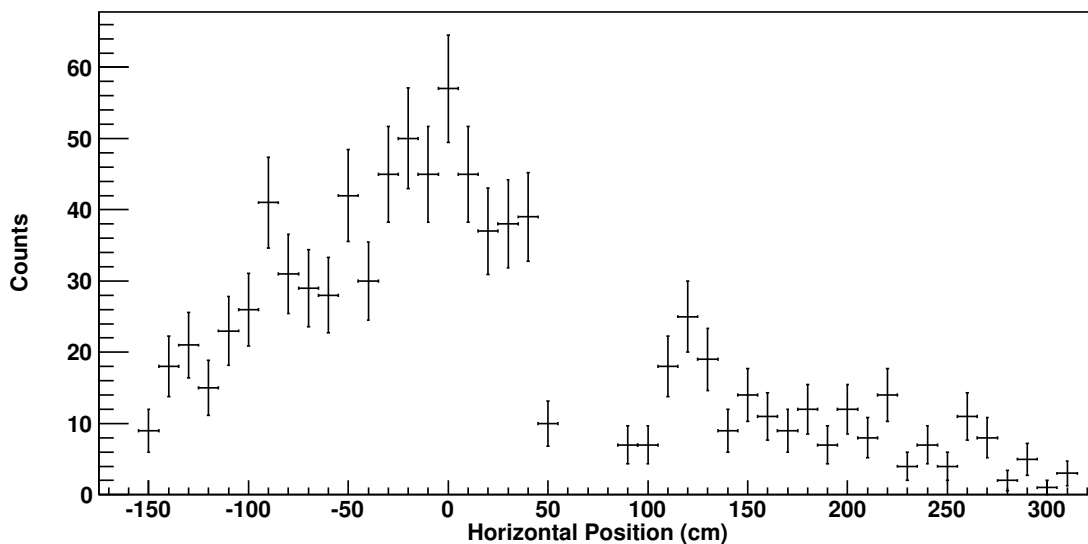


Figure 3.20: The horizontal distribution of neutron events in MoNA from the formation of ^{15}Be by neutron pick-up from the target.

3.4 Invariant Mass Reconstruction

The strategy of this experiment was to use invariant mass reconstruction to determine the decay energy of the neutron unbound state in ^{15}Be . Invariant mass spectroscopy was discussed in Section 2.1 in greater detail. The equation used to determine the decay energy is:

$$E_{decay} = \sqrt{m_f^2 + m_n^2 + 2(E_f E_n - p_f p_n \cos\theta)} - m_f - m_n \quad (3.6)$$

where m_f , E_f , and p_f are the mass, energy and momentum of the fragment, respectively. Similarly, m_n , E_n , and p_n are the values for the neutron. The angle between the velocity vector for the neutron and fragment is θ . For the neutron calculating the energy and momentum is trivial. The angle comes from calculating the vector from the target to the interaction point, and the energy and momentum are calculated with :

$$\begin{aligned}
\gamma &= \frac{1}{1 - \frac{v^2}{c^2}} \\
E &= \gamma mc^2 \\
\vec{p} &= \gamma m\vec{v}
\end{aligned}
\tag{3.7}$$

Determining the energy and momentum of the fragment in the target is more difficult and requires reconstruction of its track through the Sweeper, as described below.

3.4.1 The Inverse Map

Determining the fragment's energy and momentum at the target involves taking parameters from after the Sweeper magnet and then transforming them into parameters at the target. The central plane of the magnetic field of the Sweeper magnet was mapped using seven Hall probes, mounted vertically, on a movable cart. The cart was moved throughout the entire area of the magnet mapping the magnetic field. Details of the mapping are available from Ref. [47].

Once a reference Hall probe measurement is recorded during the experiment, a magnetic field map for this experiment is generated using IGOR PRO [52] with the archived field measurements. The field is calculated for the mid-plane of the 14 cm gap and then imported into COSY INFINITY [53] along with the fragment's charge and mass to yield a transformation matrix from the target position to the position of CRDC 1.

The matrix, M^4 , relates the particle's position and angles at CRDC1 to the angles and energy at the target. Equation 3.8 shows the relations between the parameters at the CRDC1 and the target.

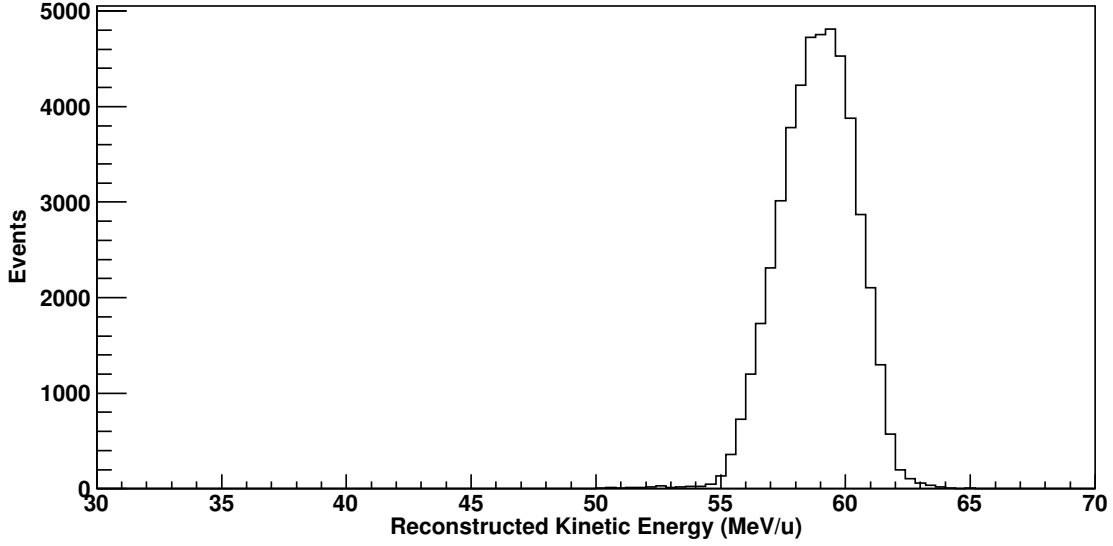


Figure 3.21: Reconstructed kinetic energy spectrum which is used to test the inverse map. The data comes from a no target run that was bent into the center of the focal plane box. The reconstructed energy is in complete agreement with the value predicted by LISE++ of 59 MeV/u

$$\begin{pmatrix} x^{crdc1} \\ \theta_x^{crdc1} \\ y^{crdc1} \\ \theta_y^{crdc1} \end{pmatrix} = M^4 \begin{pmatrix} \theta_x^{target} \\ y^{target} \\ \theta_y^{target} \\ E^{target} \end{pmatrix} \quad (3.8)$$

To accomplish the 4-parameter inversion COSY INFINITY assumes that the fragment passes through the target at zero. This assumption does increase the uncertainty about the fragment's energy and angle at the target. To account for the increased uncertainty for the experimental data, the same 4-parameter transformation was also used in the simulation. COSY INFINITY creates the transformation matrix, M^4 , which converts the quantities at CRDC1 into y^{target} , θ_x^{target} , θ_y^{target} , and E^{target} .

To check the inverse map, data from when the unreacted beam was bent into the center of

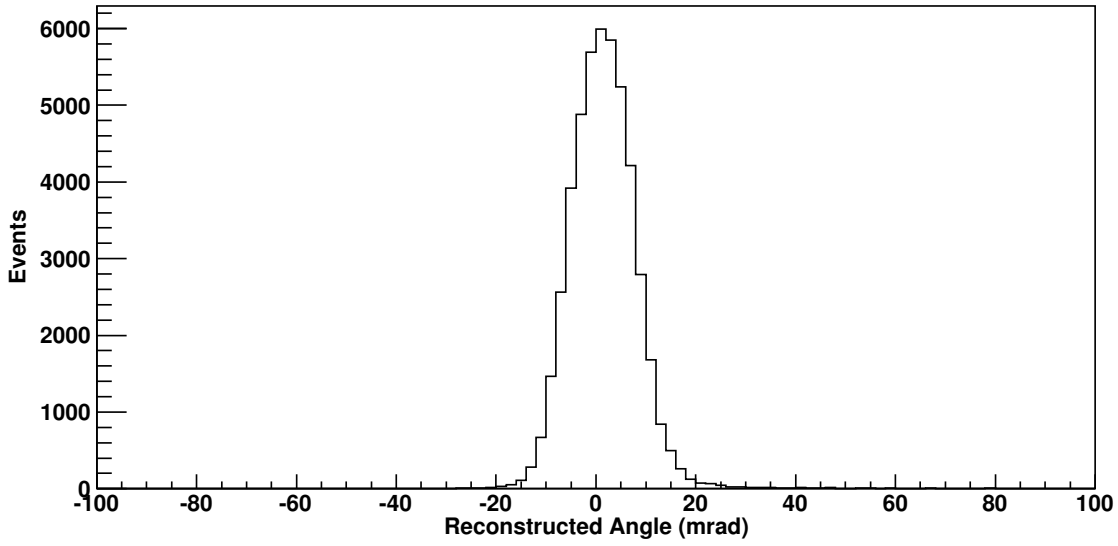


Figure 3.22: Reconstructed angle spectrum that is used to test the inverse map. The data comes from a no target run that was bent into the center of the focal plane box. The reconstructed angle is centered, confirming that the inverse map is working properly.

the focal plane box was used. The first test of the inverse map is to compare the reconstructed energy to the expected value. LISE++ calculates the average energy should be 59 MeV/u, which is in great agreement with the value from Fig 3.21.

The second test, which is more sensitive, is to check the reconstructed angle which should be centered at zero. Fig 3.22 shows the reconstructed angle is centered at approximately zero, for a no-target run that was bent into the center of the focal plane box.

3.4.2 Decay Energy

The full reconstruction of both the fragment and the neutrons gives all the parameters necessary to perform an invariant mass reconstruction using Eq. 2.6. In Fig 3.23 the black data points give the reconstructed decay energy for ^{14}Be and coincidence neutrons. The decay energy spectra is dominated by a resonance at approximately 2 MeV and the histogram contains approximately 700 total events.

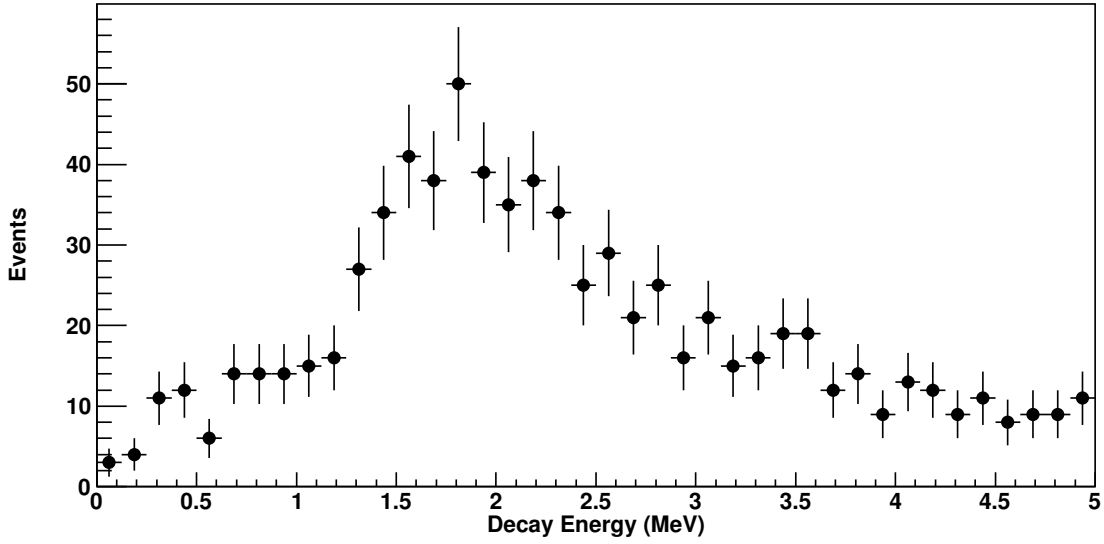


Figure 3.23: Decay energy spectrum for coincidence ^{14}Be and a neutron is shown by the black data points with their statistical uncertainty. The spectrum was calculated using Eq. 2.6. A resonance can clearly be seen at approximately 2 MeV.

3.4.3 Effect of the Carbon in the Deuterated Polyethylene

A deuterated polyethylene target was selected to maximize the number of nuclei that the ^{14}Be could interact with, while minimizing energy loss in the target. With the deuterated polyethylene target, ^{14}Be can interact with either a deuterium or a carbon atom to form ^{15}Be . To investigate any difference between reactions caused by either of these nuclei a 300 mg/cm^2 carbon target was used for approximately 10% of the experiment. As shown in Fig 3.24 the decay spectra for reactions coming from carbon (red data points) and deuterated polyethylene (black data points) are statistically identical. This indicates that invariant mass reconstruction is independent of which atom the neutron came from.

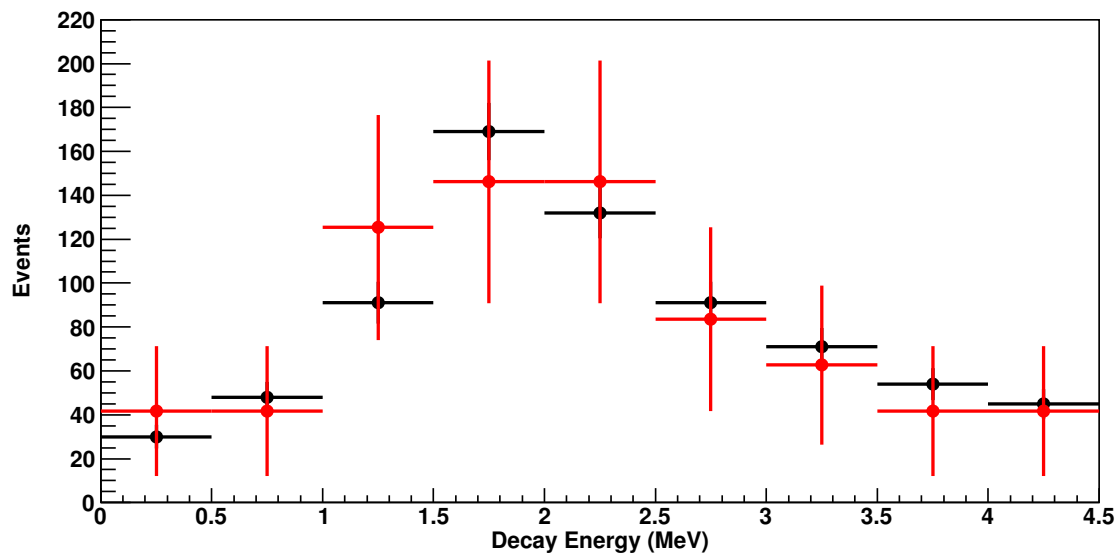


Figure 3.24: Decay energy spectrum for deuterated polyethylene and a carbon target. A 300 mg/cm^2 carbon target was used for 16 hours, the decay energy for the carbon target (red data points) is compared to the deuterated polyethylene target (black data points). The gates and conditions used to select and calibrate for both targets were the same and the results are statistically identical.

Chapter 4

Simulations

The decay energy depicted in Fig. 3.23 has the detector resolutions, acceptances, and gate conditions folded into the observed shape. To extract results, two Monte Carlo method simulation programs are employed. The first is ST MoNA, which simulates the secondary beam profile, energy loss in the target, the reaction, propagating the residual charged fragment through the Sweeper magnet, and into the charged particle detector suite. The second is Geant4, which takes the neutron's energy and angle from ST MoNA at the target and propagates it through the Sweeper and into MoNA. This Monte Carlo simulation is used to understand how the neutron interacts within MoNA.

4.1 ST MoNA

ST MoNA is a Monte Carlo simulation program [55]. The initial parameters such as energy and direction of the particle are inputs into ST MoNA. The particle then interacts at a random point within the target. For the present experiment a neutron pick-up reaction from the deuterium in the target was simulated to a state in ^{15}Be . The state immediately decays through neutron emission with the decay energy coming from an energy dependent Breit-Wigner distribution, which will be described in further detail in Section 4.1.5. The neutron's energy and direction are then fed into the Geant4 simulation. The charged particle is propagated through the Sweeper magnet using a forward transformation matrix (see Sec-

tion 3.4.1). The charged particle passes through both CRDCs and into the thin scintillator. Particles that fall outside the geometric acceptance of the detectors are eliminated from the analysis. The output data of the simulation are recorded in the same form as experimental data, allowing direct comparison between simulation and experimental data.

4.1.1 Initial Parameters

The beam profile parameters used as input into the simulation are listed in Table 4.1; these are the beam energy, location (x,y), and incident angle (Θ_x, Θ_y).

Table 4.1: The centroid and width of the gaussian distribution used to match the beam profile.

Parameter	Centroid	σ
Energy	59.05	0.0215 Mev/u
x	0	3 mm
Θ_x	0	4.5 mrad
y	0	6 mm
Θ_y	0	3.25 mrad

The beam profile was determined by removing the target and measuring the beam's position and angles in the CRDCs. In Fig. 4.1, the data (black points) are compared to the ST MoNA simulation (blue line) for the CRDC1 horizontal position, horizontal angle, vertical position, and vertical angle are shown in the top left, top right, bottom left, and bottom right panel, respectively.

Once the beam profile was known the deuterated polyethylene target was inserted and the target's thickness was varied until the location in ST MoNA matched the experimental data. The target thickness necessary to recreate the energy loss in ST MoNA was 435 mg/cm² which compares favorably with the expected thickness of 440 mg/cm².

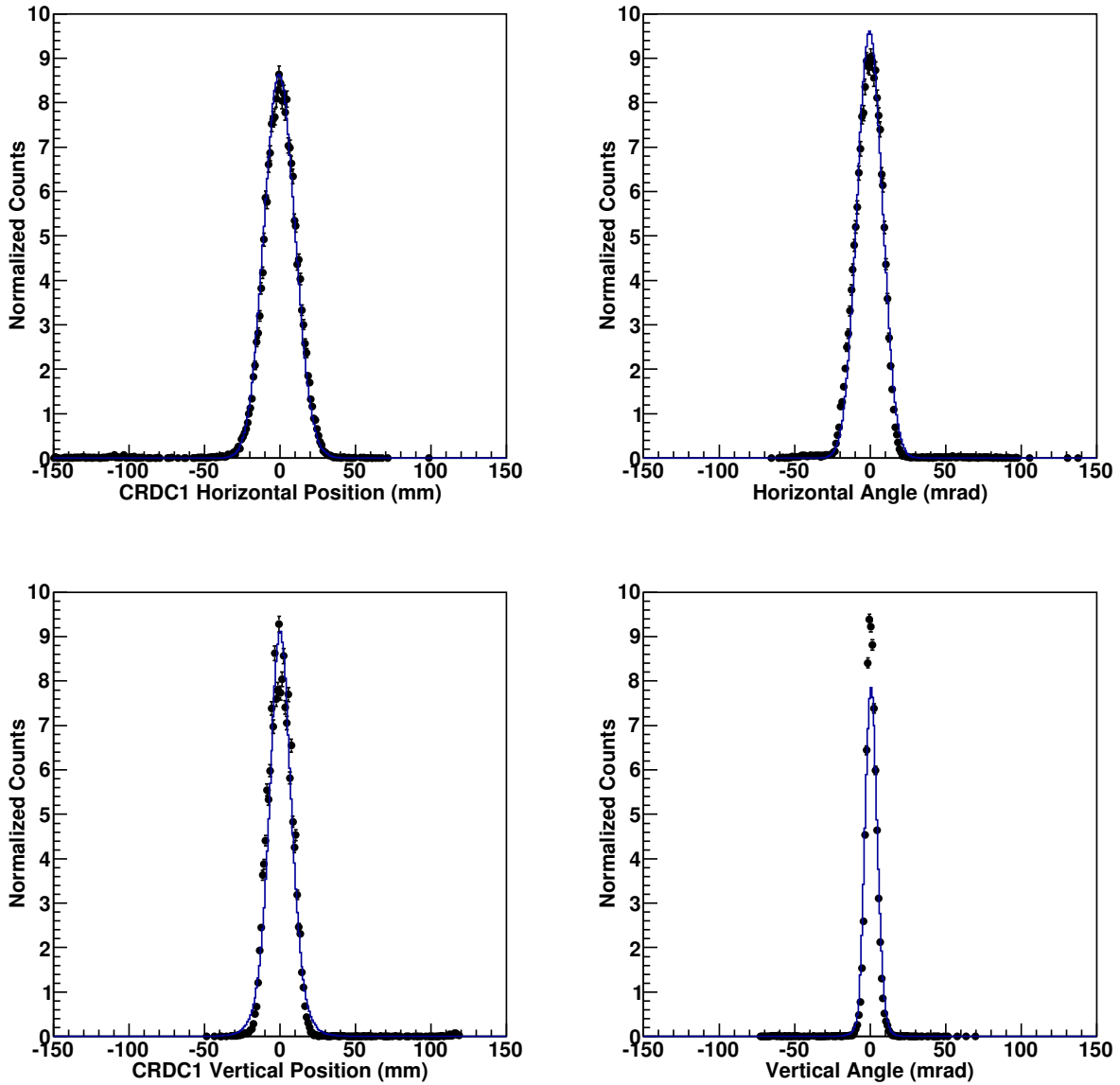


Figure 4.1: CRDC position and angle spectrum. Each figure compares data (dot) to ST MoNA simulation (line). The top left, top right, bottom left, and bottom right panel shows the comparison for the CRDC1 horizontal position, horizontal angle, vertical position, and vertical angle, respectively.

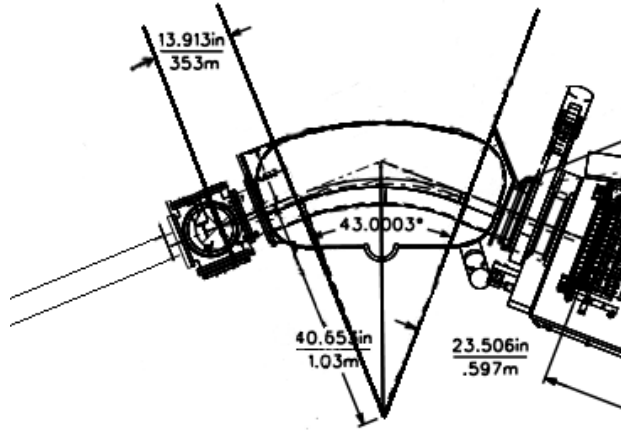


Figure 4.2: A technical drawing of the beam-line from the target to the focal plane box. The central track length from the target to CRDC1 can be determined using this diagram.

4.1.2 Central Track Length Issues

After the beam profile was matched with the beam sent into the center of the focal plane box, it was checked against step sweepers where the magnetic field was changed to illuminate the entire focal plane box. Near the center the simulated step sweeps matched reasonably well; but as the distance from the center increased the discrepancy between simulated and experimental data became apparent. The maps used in propagating the charged particles in ST MoNA from the target to CRDC1 and to reconstruct y^{target} , θ_x^{target} , θ_y^{target} , and E^{target} have the central track length as an input. Figure 4.2 is a technical drawing that includes lengths for the central track from the target to CRDC1. When those lengths are summed the total central track should be 172.3 cm. However, the map creation script has a drift distance of 7.5 cm from the target to where the map takes effect, and the map has a central track length of 157.9 cm. Adding these yields a total central track length of 165.4 cm. This constitutes a difference in distance of 6.9 cm.

To check which central track distance is accurate, maps were made with the total central track being 165.4 and 172.3 cm for different magnet settings used during the experiment.

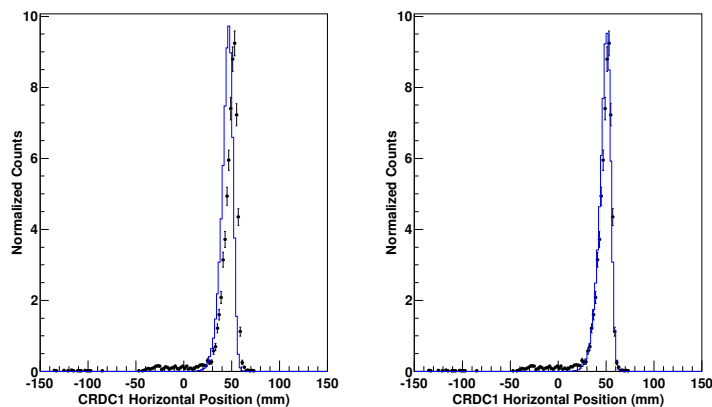


Figure 4.3: Experimental and simulation data obtained with the Sweeper magnet’s current at 366 A. The blue line represents an ST MoNA simulation, while black points represents experimental data. The left panel reflects a simulated total central track length of 165.4 cm and the right panel uses 172.3 cm.

The maps with a total central track length of 172.3 cm were made with a 7.5 cm initial drift distance from the target to where the magnetic field takes affect, a central track length in the magnetic field of 157.9 cm, and an additional drift distance of 6.9 cm to CRDC1. Figure 4.3 shows the Sweeper magnet set to 366 A with the data represented as black points. The left hand panel shows the blue ST MONA simulation where the map used to propagate the unreacted beam to the target has a total central track length of 165.4 cm. The right hand panel blue line is a ST MoNA simulation where the total central track length is 172.3 cm. The magnet’s current was set to 306, 316, 326, 336, 356, 366, and 371 A, which illuminated the entire sweeper focal plane box’s acceptance when the 440 mg/cm² deuterated polyethylene target was in place. For every current setting, the total central track length needed to be increased to line up the centroid of simulation data with the step sweep data. The distance necessary varied randomly from 5 to 15 cm with a mean of 9(3) cm. A total central track length of 172.3 cm, which corresponds to the central track length from Fig 4.2, was used for all analysis presented in this thesis.

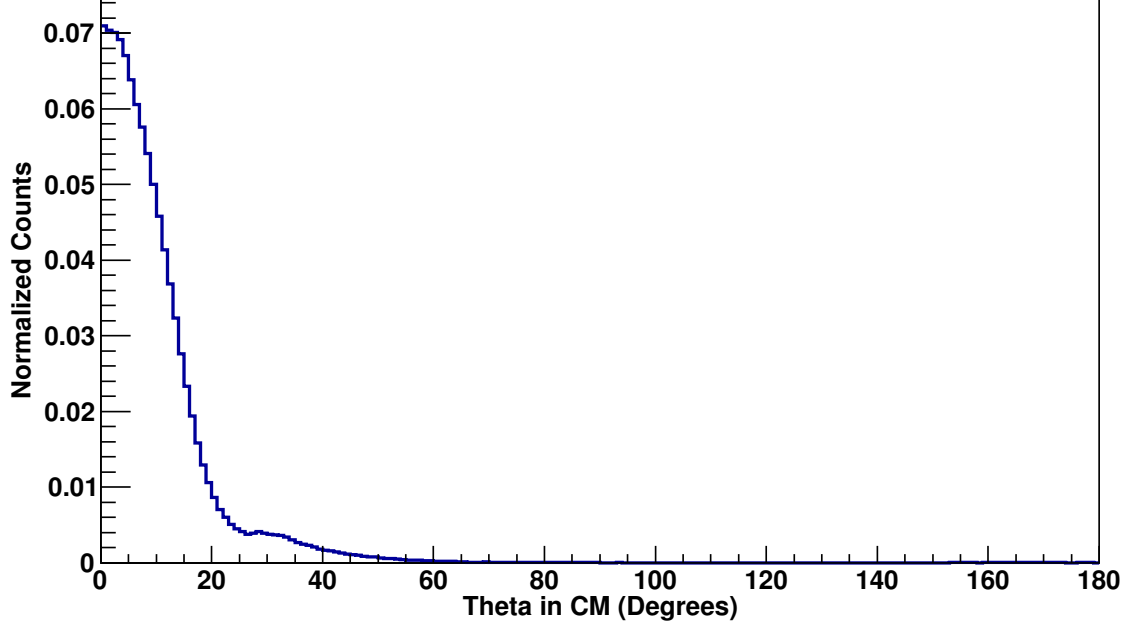


Figure 4.4: Angular distribution of the reaction used in ST MoNA, calculated with FRESCO using the global optical potentials from Refs. [38, 35].

4.1.3 Final Checks

In Section 4.1.1 it was shown that the incoming beam profile used in ST MoNA was in good agreement with data from unreacted ^{14}Be centered in the focal plane box. The final check is to implement the reaction mechanism in ST MoNA and compare the results to the experimental data. This provides a check of the neutron pick up model to simulation the reaction.

The reaction was modeled as ^{14}Be picking up a neutron from the deuterium and forming ^{15}Be , which immediately decays back into ^{14}Be and a neutron. Figure 4.4 shows the angular distribution as calculated by FRESCO [33] using the global optical potential from Refs. [38, 35]. The decay energy distribution is calculated with Eq. 4.1.

Figure 4.5 provides a comparison of simulation (blue line) to data (black points) at CRDC1 for ^{14}Be reaction products. Figure 4.6 provides the same comparisons for parameters

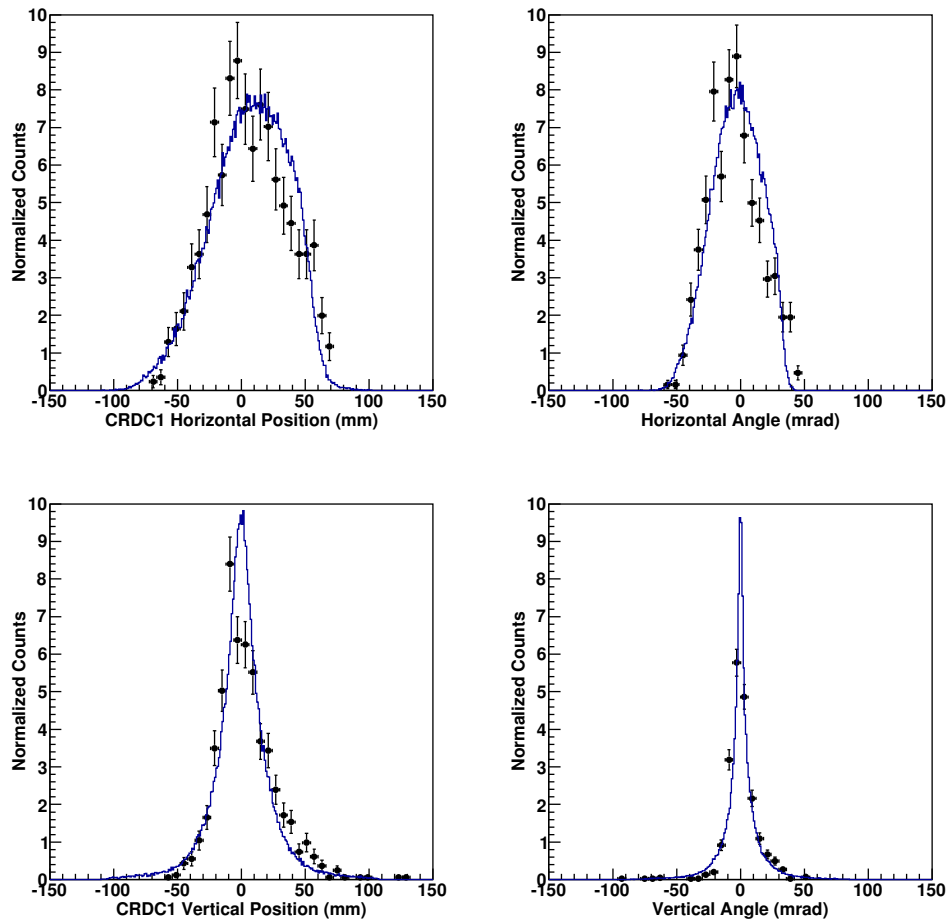


Figure 4.5: Comparison of simulation (blue line) to data (black points) for ^{14}Be reaction products located in the focal plane. The parameters are compared are CRDC1 X, Θ_X , Y, and Θ_Y which are located in the upper-left, upper-right, lower-left, and lower-right panel, respectively.

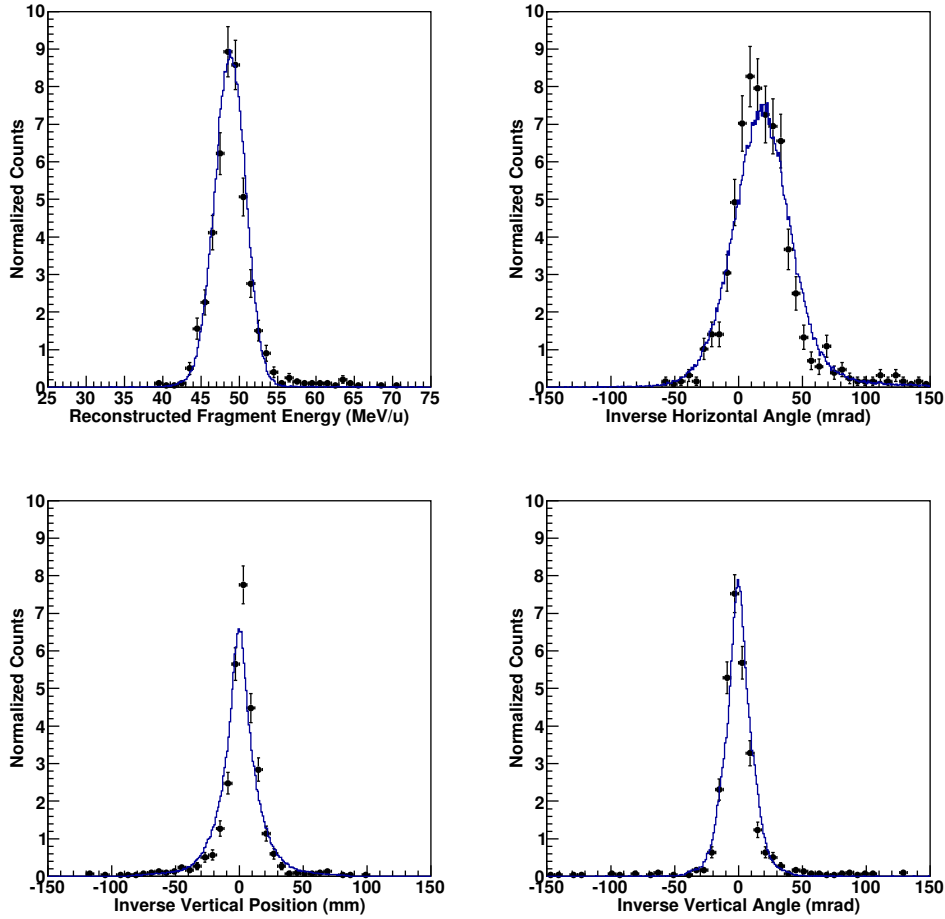


Figure 4.6: Comparison of simulation (blue line) to data (black points) for ^{14}Be reaction products located in the focal plane. The parameters are compared are target E , Θ_X , Y , and Θ_Y which are located in the upper-left, upper-right, lower-left, and lower-right panel, respectively.

at the target created where the inverse mapping procedure(see Section 3.4.1) was applied to the data and the simulation. There is reasonable agreement between simulation and data for all measured parameters, confirming the reaction mechanism.

4.1.4 Geometric Efficiency

Figure 4.7 shows the geometric efficiency of the MoNA and Sweeper system. This efficiency does not include the intrinsic efficiency of MoNA and the charged particle detectors. It was

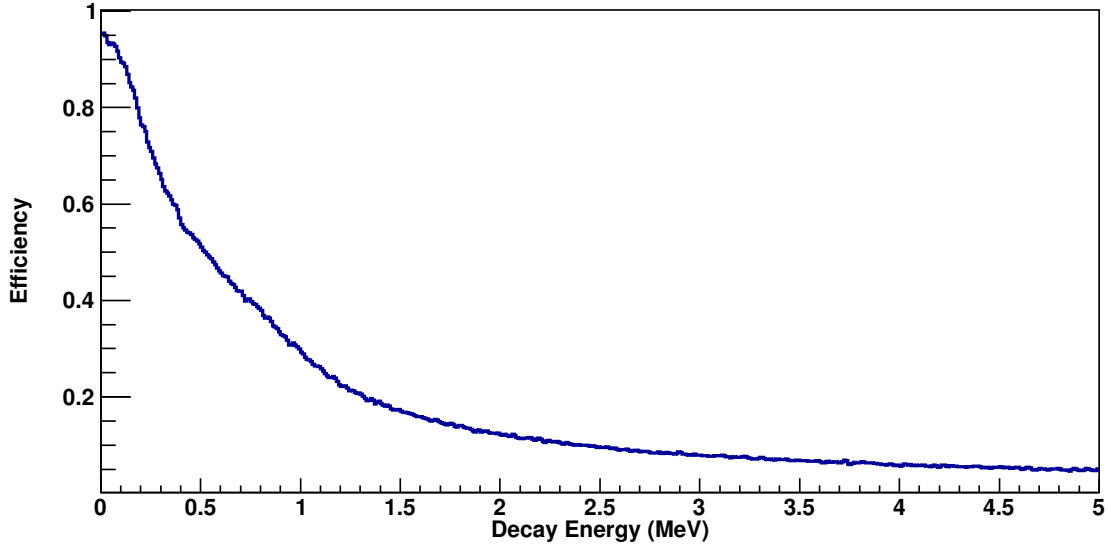


Figure 4.7: Geometric efficiency of the MoNA and Sweeper system. It was calculated for energies between 0 and 5 MeV for a neutron pick-up reaction from deuterium.

calculated with ST MoNA for decay energies between 0 – 5 MeV for a neutron pick-up reaction from deuterium.

4.1.5 Resonance Modeling

The decay of a neutron unbound resonant state is a two body problem, involving a neutron and the residual charged fragment. It can be described by the inverse reaction as a neutron scattering off a nucleus at different energies. The cross section for this process, $\sigma(E)$, is well described by R-matrix theory [56] and has the form of an energy dependent Breit-Wigner distribution [57]. For the decay only the shape of the resonances is relevant. The particular form used is:

$$\sigma \sim \frac{\Gamma_\ell(E, \Gamma_f)}{(E_0 + \Delta_\ell(E, \Gamma_f) - E)^2 + \frac{1}{4}\Gamma_\ell(E, \Gamma_f)^2} \quad (4.1)$$

E is the neutron energy; E_0 is the central resonance energy; Γ_f is called the formal width; ℓ

is the orbital angular momentum; Γ_ℓ and Δ_ℓ are described by Eq. 4.2 and 4.6.

The function Γ_ℓ is:

$$\Gamma_\ell = \Gamma_f \frac{P_\ell(E)}{P_\ell(E_0)} \quad (4.2)$$

where $P_\ell(E)$ is given by:

$$P_\ell = \frac{\rho}{F_\ell^2 + G_\ell^2} \Big|_{r=a} \quad (4.3)$$

where a is the minimum distance of approach, which is given by:

$$a = r_0(A_n^{1/3} + A_f^{1/3}) \quad (4.4)$$

and G_ℓ and F_ℓ are composed of:

$$\begin{aligned} G_\ell &= \left(\frac{\pi\rho}{2}\right)^2 J_{\ell+1/2}(\rho) \\ F_\ell &= (-1)^\ell \left(\frac{\pi\rho}{2}\right)^2 J_{-\ell-1/2}(\rho) \end{aligned} \quad (4.5)$$

$J_{\pm(\ell+1/2)}$ are J-type Bessel functions and $\rho = a\sqrt{2ME}/\hbar$. The function Δ_ℓ is given by:

$$\Delta_\ell = \frac{-\Gamma_f}{2P_\ell(E_0)} (S_\ell(E) - S_\ell(E_0)) \quad (4.6)$$

where S_ℓ is the shift function and is given by:

$$S_\ell = \rho \frac{F_\ell F'_\ell + G_\ell G'_\ell}{F_\ell^2 + G_\ell^2} \Big|_{r=a} \quad (4.7)$$

where G'_ℓ and F'_ℓ are the derivatives of Eq. 4.5 with respect to r . The approximation to the shift functions can be found in Ref. [58] and for $\ell = 1$ and $\ell = 2$ they are:

$$\begin{aligned} S_1 &= \frac{-1}{1 - (ka)^2} \\ S_2 &= \frac{-3(6 + (ka)^2)}{9 + 3(ka)^2 + (ka)^4} \end{aligned} \tag{4.8}$$

where $ka = a\sqrt{2ME}/\hbar$. It should be noted in the original paper from Lane and Thomas that Table A.1 contains a typographical error. The numerator for S_2 is listed incorrectly as $-3(6 + (ka)^4)$ instead of $-3(6 + (ka)^2)$.

4.2 Geant4

Geant4 is a software package that uses Monte Carlo methods to simulate the passage of particles through matter [59]. In the present analysis Geant4 is only used to simulate the interaction of the neutrons, while ST MoNA was used to handle the incoming beam profile, reaction in the target, propagating the charged particle through the magnetic field of the Sweeper magnet, and determining the interaction within the focal plane box detectors. ST MoNA then saves the emitted neutron's energy and direction and passes it to Geant4.

The neutron is initialized in the Geant4 framework [59, 60] and then propagated through the Sweeper magnet. The simulated magnet was created to match the dimensions of the large gap and neutron window in the Sweeper magnet. The Sweeper is made of different materials, but in Geant4 it is approximated as being solid iron.

Once the neutron is beyond the Sweeper magnet it is propagated to MoNA, where it can interact within a bar of MoNA. Each simulated bar consists of plastic with a carbon to

hydrogen ratio of 1.104 and a density of 1.032 g/cm^3 which matches BC-408 [46]. In addition, the simulated bars are wrapped with vinyl tape and have light guides at both ends. If the neutron interacts within the bar, the energy deposited is converted to light output using Birk's Law [61], and the light is attenuated as it propagates to both ends of the bar. A cut is then applied to mimic the detector threshold of 380 keVee. If the threshold was met, the time of flight and energy of each event were recorded.

Experimental data is abundant for cross sections and angular distribution for neutrons interacting with nuclei from 0–20 MeV, but from 20 to 300 MeV there is limited data available. Previous studies have shown that different techniques do not provide realistic interactions for neutrons in the intermediate energy range (20 – 300 MeV) [62, 63, 64, 65, 66, 67]. The lack of an extensive collection of experimental data in this energy range lowers the ability of simulations to accurately describe the way that neutrons interact in materials.

Below 20 MeV, Geant4 uses G4NeutronHPElastic and G4NeutronHPInelastic [70], which are based on the Evaluated Nuclear Data Files (ENDF/B–VI) [68, 69]. They contain high precision cross sections and angular distribution data for elastic and the inelastic reactions. The inelastic reaction data include detailed information about the different reaction channels. This provides a good description of neutrons below the 20 MeV, however, they are not appropriate for the present experiment where neutron energies are in the range of 40–60 MeV.

Above 20 MeV, the stock Geant4 physics classes G4HadronElasticProcess and G4LElastic are used which describe the elastic scattering of the neutron. The inelastic reactions are determined within the G4LENeutronInelastic and G4CascadeInterface classes. They are based on the pre-equilibrium Bertini intranuclear cascade model [71], followed by evaporation. Neutron interaction cross section for both the elastic and inelastic reactions are taken from the Japanese Evaluated Data Library (JENDL–HE) [72, 73]. The disadvantage of this approach

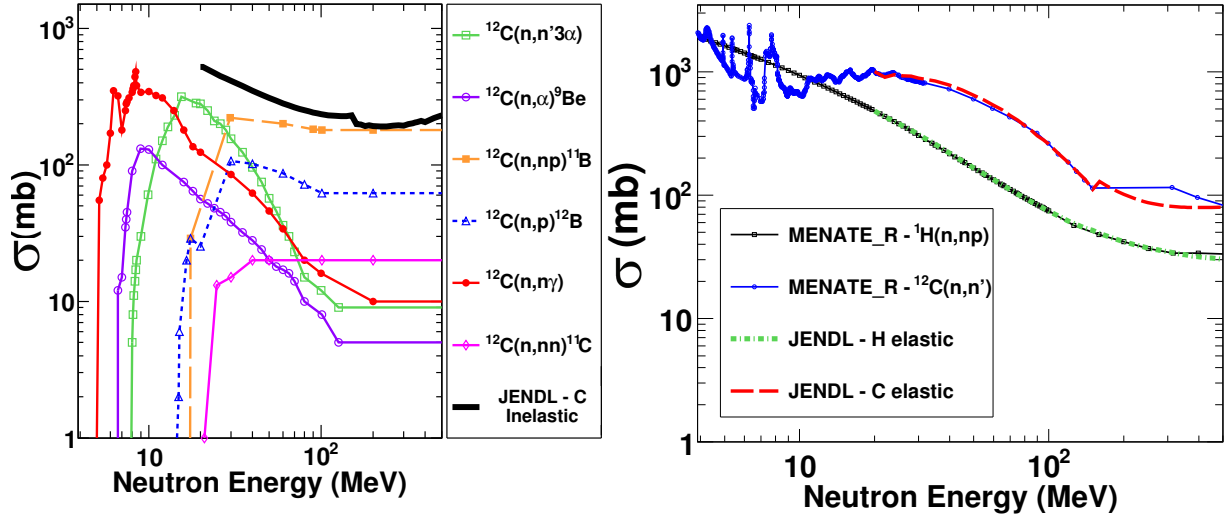


Figure 4.8: The left panel shows the total carbon–neutron inelastic reaction cross section used in the stock G4Physics class (JENDL–HE). The other six colors show the discrete inelastic reaction cross sections used in the Menate_R code. The right panel shows the hydrogen elastic cross section for G4Physics Class (Green) and Menate_R (Black). Also shown is the carbon elastic cross section for the G4Physics (Red) and Menate_R (Blue). (adopted from Ref. [79])

is that the inelastic process does not explicitly describe the different inelastic channels.

Thus, a custom neutron interaction model, Menate_R [74], was implemented in the Geant4 platform. Menate_R was originally designed to simulate neutron interaction in NE213 scintillators for the EURISOL design study [74]. Menate_R uses discrete inelastic reaction channels for the neutron interacting with carbon above 20 MeV. The interaction was incorporated into a C++ class derived from G4VDiscreteProcess to allow implementation within the Geant4 framework.

The left panel of Fig. 4.8 shows the total carbon–neutron inelastic reaction cross section from the JENDL–HE database [73] used in the stock Geant4 physics class; the other six colors represents the carbon–neutron inelastic reaction channels used by the Menate_R package. Below 20 MeV the stock G4Physics class uses the same channels as the Menate_R package, as opposed to the total inelastic cross section. The right panel of Fig. 4.8 shows a comparison of

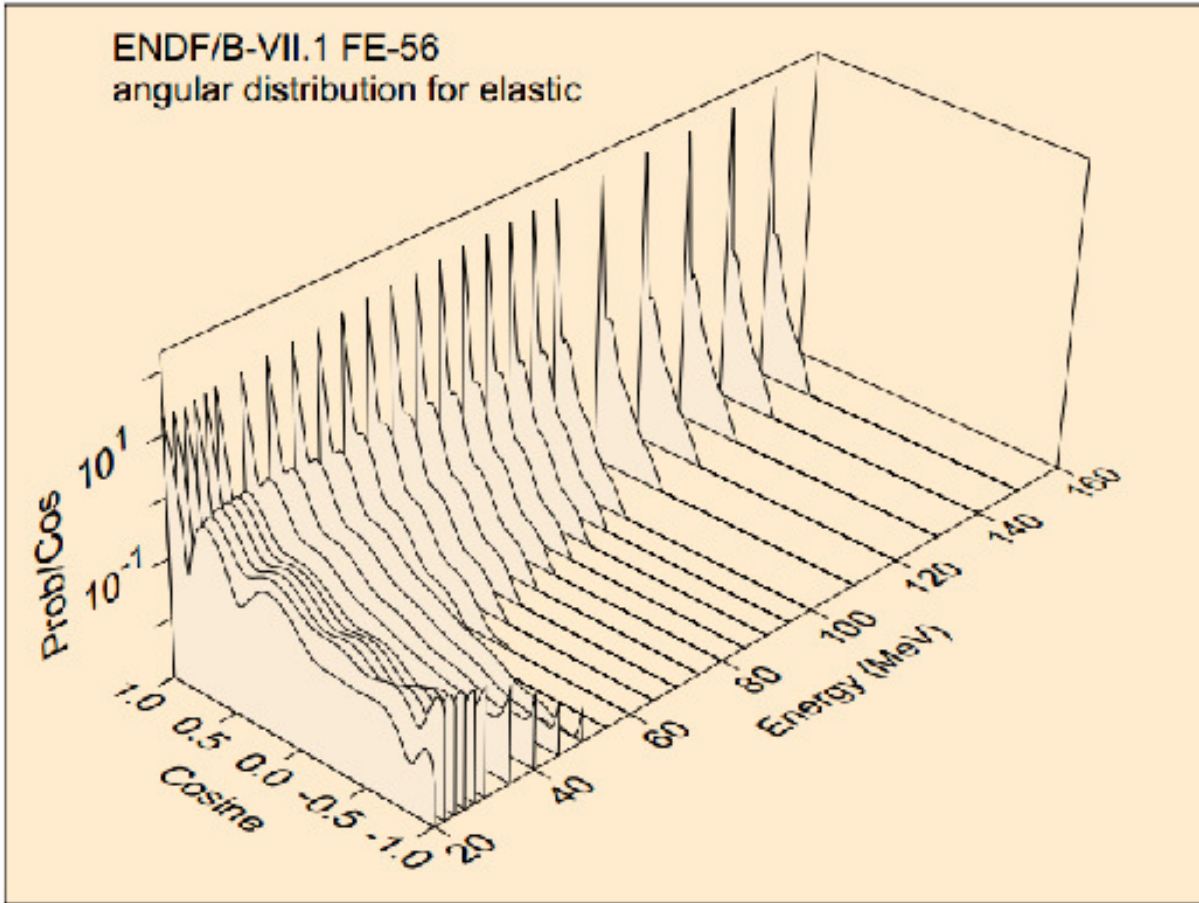


Figure 4.9: Visual representation of the elastic cross sections for iron at different energies from Ref [78]. The cross sections at 30, 50, and 70 MeV were added to Menate_R, and then extrapolated to the energy of the neutron.

the elastic hydrogen cross section used in the G4Physics class (Green) and Menate_R (Black) and the elastic carbon cross section used in the G4Physics class (Red) and Menate_R (Blue). There is no difference in the elastic cross sections in the energy range at which the MoNA-Sweeper setup is typically run.

Menate_R only calculates interactions of neutrons with carbon and hydrogen, which works well for the plastic scintillators in MoNA. To model the Sweeper magnet, the cross sections for iron had to be added to Menate_R. The cross sections were added from the ENDF/B-VI database [69] for 30, 50, and 70 MeV. Menate_R then interpolates to the energy of the

neutron. Figure 4.9 shows the elastic cross sections for iron at different energies. Menate_R assumes that the neutron is absorbed if it interacts inelastically with iron. Aluminum cross sections were also added to the code for possible use in future studies.

4.2.1 Comparison

To check the two interaction models used in Geant4 it is necessary to compare them to an experiment where the results are easily understood. This requires an experiment that populates a neutron unbound state that only emits a single neutron. Such an experiment was a one proton knockout of ^{17}C populating the ground state of ^{16}B which decayed to the ground state of ^{15}B . Complete details of the experiment can be found in Ref. [77]. For every ^{15}B present, there should be only a single neutron, thus any multiple interactions must come from the scattering of that single neutron.

The major observable difference can be seen in the left panel of Fig. 4.10 which shows the multiplicity of the experimental data (Black) compared with G4Physics (Red) and Menate_R (Blue). The figure has been normalized at multiplicity = 1. G4Physics, across the board, grossly overestimates the multiplicity compared to the experimental data and the Menate_R model. The right hand panel of Fig. 4.10 shows the energy deposited for the experimental data (Black), G4Physics (Red), and Menate_R (Blue). G4Physics over represents the high and low energy deposited, while Menate_R effectively reproduces the data. Figure 4.10 demonstrates that the stock G4Physics class is inferior to the Menate_R package in describing the intermediate energy range neutron interaction within MoNA.

Since the multiplicity and deposited energy are produced from interactions in MoNA, and the elastic scattering cross sections used are nearly identical for both models, it implies that the difference is due to the inelastic reactions. The cascade model used in the G4Physics

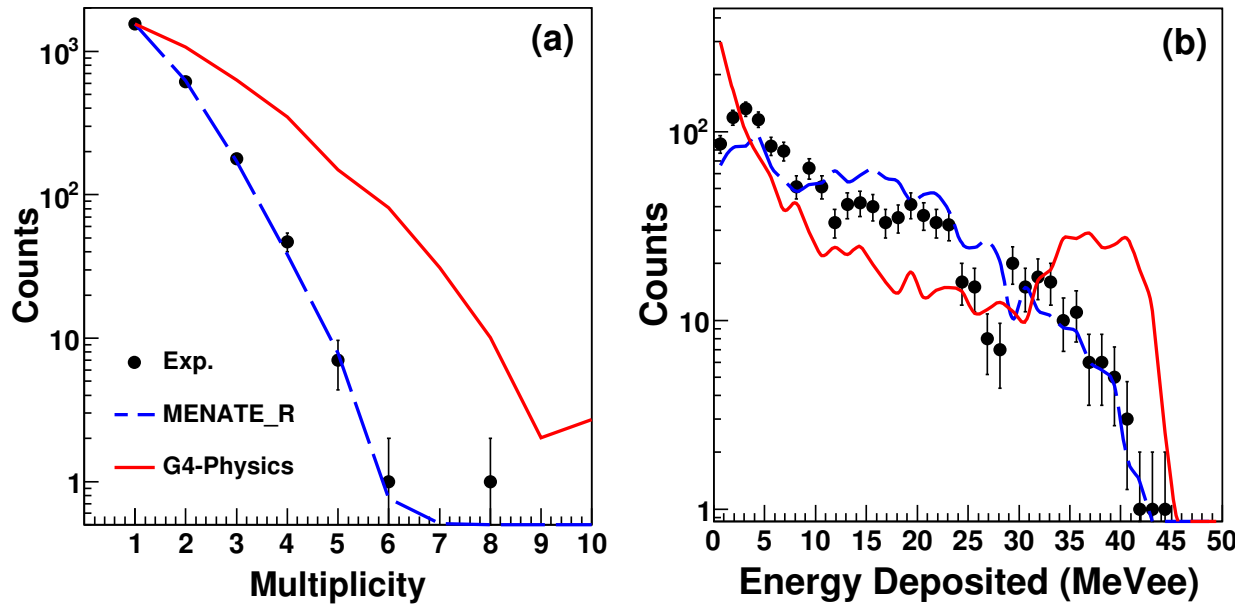


Figure 4.10: Experimental data (Black) from Ref. [77] is compared to the G4Physics (Red) and Menate_R (Blue) model. The left panel shows the multiplicity and right panel shows the energy deposited. In the left panel the multiplicity distributions were normalized so that multiplicity = 1 events matched. The right panel was normalized for total number of events. (adopted from Ref. [79])

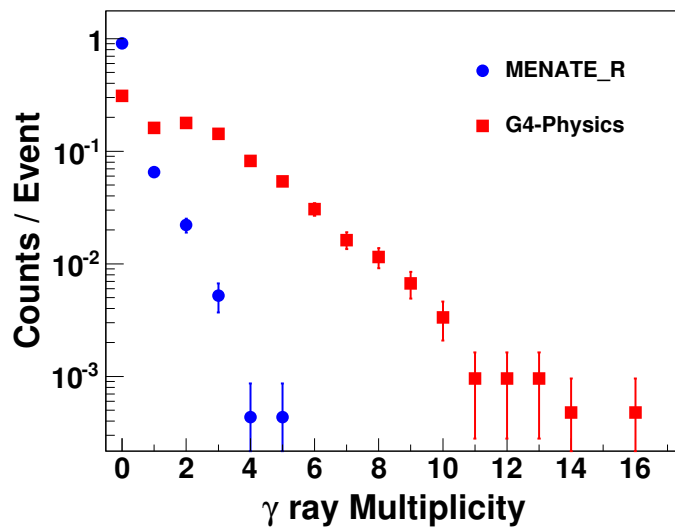


Figure 4.11: Comparison between the stock G4Physics (Red) and Menate_R (Blue) models of multiplicity distribution for interactions within MoNA where γ rays are produced from inelastic reactions with carbon. (adopted from Ref. [79])

dramatically overproduces γ rays relative to $^{12}\text{C}(n, n\gamma)$ inelastic reaction channel within Menate_R. This can lead to γ rays that are produced in one bar propagating to another and inducing an interaction, which can drastically increase in multiplicity produced by the G4Physics model and the increase of low energy events that are observed. The multiplicity of γ rays produced through inelastic scattering with carbon is shown in Fig. 4.11. It should be noted that this is not likely the sole cause of the observed discrepancy, but it accounts for much of the difference. Further verification of the Menate_R model can be seen in Ref. [79].

Chapter 5

Results

This experiment represents the first time ^{15}Be was observed experimentally, allowing for the measurement of the resonance observed in Fig. 3.23 and calculation of the cross sections for neutron transfer from carbon and deuterium to ^{14}Be .

5.1 Resonance Energy

The measured decay energy spectrum for $^{14}\text{Be} + n$ coincidences resulting from the decay of ^{15}Be unbound states is presented in Fig. 5.1. The experimental decay energy spectrum was fitted using an energy dependent Breit-Wigner distribution (see Eq. 4.1) which assumed an $l = 2$ decay along with a background contribution. The background is most likely due to the population of unbound, higher-lying states. Other than the peak close to 2 MeV, no distinct resonance features were apparent. The background was approximated with a combination of $l = 0$ and $l > 0$ components. These contributions were selected to reproduce the background below 1 MeV and above 3 MeV, respectively. The $l = 0$ line shape (red long dashes) in Fig. 5.1 was calculated using the analytic approximation, which comes from Ref. [80]:

$$\frac{d\sigma}{d\epsilon} \sim \frac{1}{k} \left(\frac{k \cos(a_s k) - \gamma \sin(a_s k)}{\gamma^2 + k^2} \right)^2 \quad (5.1)$$

where a_s is the scattering length, $\gamma = \sqrt{2m\epsilon_B}$, ϵ_B is the binding energy of ^{14}Be , $k = \sqrt{2m\epsilon_f}$,

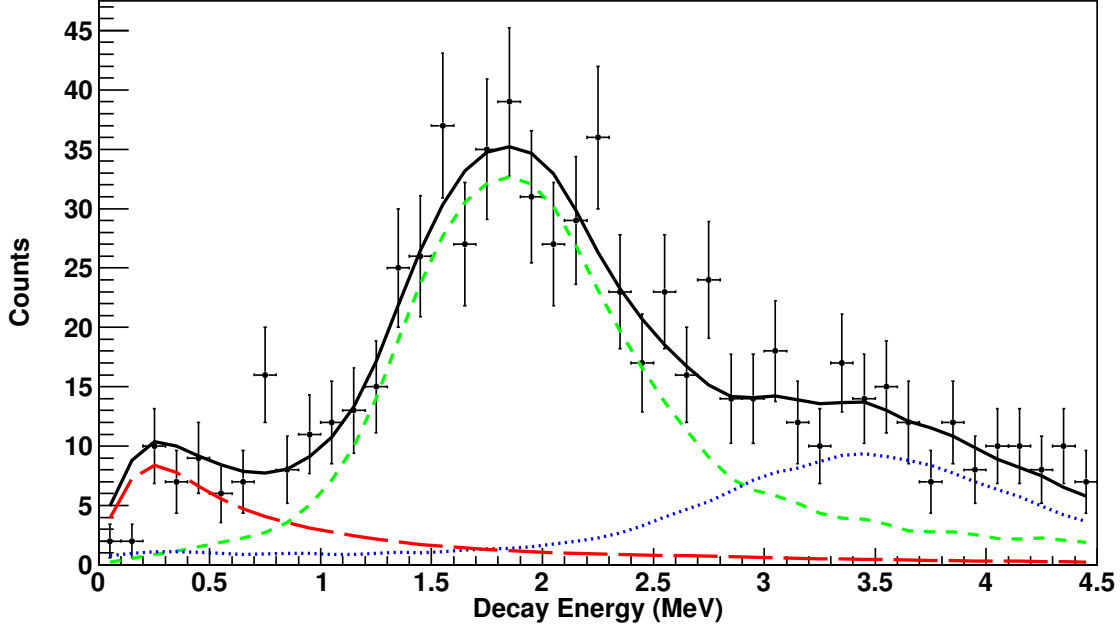


Figure 5.1: ^{15}Be decay energy spectrum. The data are shown by the black data points with statistical error bars. The best fit to the data (solid black line) is a sum of an $l = 2$ resonance (green short-dashed line) and background contributions approximated by $l = 0$ (red long-dashed line) and $l > 0$ (blue dotted line) components.

and ϵ_f is the decay energy of the neutron. NuShellx predicts a $1/2^+$ state at 3.5 MeV in ^{15}Be that will decay through an $l = 0$ neutron emission to the ground state in ^{14}Be , corresponding to a scattering length of -2.5 fm. To reproduce the background above 3 MeV a Breit-Wigner line shape was used with a centroid of 3.5 MeV with a width of 0.8 MeV (blue dots). The overall fit was not sensitive to the detailed parameterizations of the background contribution. Thus, these fit parameters should not be interpreted as distinct states in ^{15}Be .

For the final fit the $l = 2$ resonance energy, width, and normalization, along with the normalization of the two background contributions were free parameters. The best fit to the data is shown by the black solid line in Figure 5.1; it was achieved with a resonance energy of 1.8 ± 0.1 MeV and a width of 575 ± 200 keV along with the two background components. The individual contributions of the $l = 2$ resonance, and the $l = 0$ and $l > 0$ background

contributions are shown by the green short-dashed, red long-dashed, and blue-dotted lines, respectively. The resonance accounted for 531 of the 768 observed events in the decay spectra. This observation corresponds to the first identification of the neutron-unbound nucleus ^{15}Be . The observation of the $5/2^+$ state at 1.8 MeV above the ground state of ^{14}Be , which has a mass excess of 39.95 ± 0.13 MeV [81], means that ^{15}Be has a mass excess of 49.82 ± 0.16 MeV. The experimental mass excess for ^{15}Be is consistent with the value from the 2012 atomic mass evaluation of 49.76 ± 0.4 MeV [81].

Shell model calculations with NUSHELLX, mentioned in the introduction, predicted the $3/2^+$ ground state and the $5/2^+$ excited state to be separated by only 300 keV. It is conceivable that the observed peak corresponds to a sum of both of these states, however this is not required by the data. The extracted width of the single-component fit, 575 ± 200 keV, is consistent with the calculated single-particle width of 405 keV which was derived from:

$$\Gamma_{sp} = \frac{2\hbar^2}{MR^2}(kR) \frac{2\ell - 1}{2\ell + 1} T_\ell(kR) \quad (5.2)$$

where $R = 1.13A^{1/3}$ fm is the nuclear radius, M is the reduced mass, $k = \sqrt{2ME}/\hbar$, and the transmission probability, $T_\ell(kR)$, is given by:

$$T_2(kR) = \frac{(kR)^4}{9 + 3(kR)^2 + (kR)^4} \quad (5.3)$$

The neutron configuration presented in Section 1.1 indicate that the $5/2^+$ state should be populated significantly more than the $3/2^+$ state and that the $5/2^+$ state has substantial spectroscopic strength for decaying to the ground state of ^{14}Be , whereas the $3/2^+$ state will predominantly decay to the first excited 2^+ state of ^{14}Be . Thus, the resonance observed in Fig 5.1 is tentatively assigned to the $5/2^+$ state.

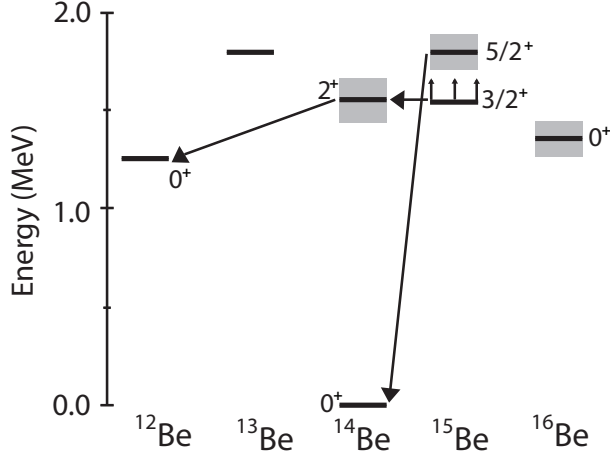


Figure 5.2: Partial experimental level scheme for neutron rich beryllium isotopes. The height of the gray boxes represents the uncertainties of the states. The data for the excited state in ^{14}Be is from [26], the lower limit for the $3/2^+$ is from [17], the ^{15}Be $5/2^+$ state is from the present work and the two-neutron separation energy for ^{16}Be is from [13].

The current experiment does not resolve the question which of the two states corresponds to the ground state. Figure 5.2 summarizes the experimental status of the neutron-rich beryllium isotopes. The non-observation of ^{14}Be in the two-proton knock-out experiment established a lower limit for the decay energy of the $3/2^+$ state of 1.54 MeV [17]. This state will decay to the unbound first excited 2^+ state of ^{14}Be which then subsequently will decay via two neutron emission to the ground state of ^{12}Be . It will be difficult to observe because it will require the kinematic reconstruction of three neutrons. The present results observe the $5/2^+$ state at a decay energy of 1.8 ± 0.1 MeV. As shown in Figure 5.2, this places the ^{15}Be state above the ^{16}Be ground state by 450 ± 140 keV, reducing its contribution as a possible intermediate step for the sequential decay from ^{16}Be significantly.

5.2 Cross Section

In addition to measuring the decay energy, it is possible to calculate the cross sections for the $^{14}\text{Be}(\text{d,p})^{15}\text{Be}$ and $^{14}\text{Be}(^{12}\text{C},^{11}\text{C})^{15}\text{Be}$ reactions. The cross section, in millibarns, is calculated by:

$$\sigma = \frac{n_r 10^{27}}{n_b n_t} \quad (5.4)$$

where n_r , n_b , and n_t represent the total number of reactions, beam particles, and target nuclei per cm^2 , respectively. The number of target nuclei was determined using:

$$n_t = \frac{N_A t_t}{A} \quad (5.5)$$

where $N_A = 6.02 * 10^{23} \text{ mol}^{-1}$ is Avogadro's number, t_t is the thickness of target in units of g/cm^2 , and A is mass in units of atomic mass. The calculation is straightforward for the carbon target but for the deuterated polyethylene target it is also necessary to calculate the fraction of deuterium to hydrogen in the target (see Section 5.2.3).

The number of beam particles, n_b , was not measured directly. Instead n_b was deduced by calibrating the scalers of the target scintillator (tss) with a run where the unreacted beam (urb) was centered in the focal plane box without a target. In this run the same gates were used as in the reaction data (beryllium gate on the incoming beam, padsum gate on both CRDCs, and the beryllium gate after the sweeper magnet), removing the effects of the incoming beam's purity and efficiencies of the charged particle detectors.

$$n_b = \epsilon_{lt} n_{tss} * \frac{n_b^{urb}}{\epsilon_{lt}^{urb} n_{tss}^{urb}} = 0.58 \epsilon_{lt} n_{tss} \quad (5.6)$$

where ϵ_{lt} is the live time as determined from the scalers, and n_{tss} is the number of events recorded in the target scintillator's scaler.

The number of reactions populating the resonance was calculated as:

$$n_r = \frac{n_s}{\epsilon_d \epsilon_a \epsilon_{lt}} \quad (5.7)$$

where n_s is the number of events in the decay spectra within the 1.8 MeV resonance divided by the efficiencies of the setup. The live time, $\epsilon_{lt} = 0.99$, was determined directly from the scalers. The detector efficiency, ϵ_d , was determined to be $\epsilon_d = 0.0712$ with an uncertainty of 20% and corresponds to the acceptances and the intrinsic efficiency. The detector efficiency was determined using a combination of Monte Carlo simulations provided by ST_MONA and GEANT4. It should be noted that the efficiencies of the charged particle detectors were taken into account in the total incoming beam particle calculations. The analysis efficiency, ϵ_a , was based on the gate shown in Fig. 3.16. The effects from this cut was estimated to be $\epsilon_a = 0.67$ with an uncertainty of 20%.

5.2.1 Systematic Uncertainty

The individual contributions to the systematic uncertainty are listed in Table 5.1. The analysis and detector efficiency uncertainty were both discussed at the end of the previous section. Another uncertainty is due to the reaction mechanism used in the simulation. The angular distribution of the fragments was deduced from the differential cross sections calculated by FRESCO (see Fig. 4.4). The Sweeper magnet acceptance for angular distributions calculated from three different optical potentials [36, 37, 38] differed by no more than 5%. The uncertainty of the target thickness was estimated to be 2% and 15% for the carbon and

Table 5.1: The sources of the systematic uncertainty.

Source	Carbon Target (%)	CD2 Target (%)
Analysis Efficiency (ϵ_a)	10	10
Detector Efficiency (ϵ_d)	20	20
Differential Cross Section	5	5
Target Thickness	2	15
Total	37	50

deuterated polyethylene, respectively. The latter will be discussed in more detail in Section 5.2.3. The errors listed in Table 5.1 correspond to the average error and the total relative error is calculated from the sum of these relative errors.

5.2.2 Carbon Target

The cross section for neutron pick up from carbon was determined by using a $t_{t,carbon} = 308 \text{ mg/cm}^2$ carbon target for 16 hours. From Fig. 3.24 it can be seen that the decay energy spectra for the carbon target was statistically identical to the deuterated polyethylene target. Due to the limited statistics it was not possible to fit the resonance and separate it from background contributions. Thus the total number of events in the spectrum was scaled by the ratio of the resonance contribution (531 ± 23) to the total events (791 ± 28) for the deuterated polyethylene target resulting in $n_s = 18 \pm 4$. The total number of reactions can then be calculated to be, $n_r = 380 \pm 75$. Using Eq. 5.5 with a carbon target thickness of $t_t = 0.308 \text{ g/cm}^2$ gives the total number of target nuclei $n_t = 1.545 * 10^{22}$. The number of incoming beam particles was $n_b = 2.29 * 10^7$. The cross section for neutron transfer from the carbon target was then $\sigma_{carbon} = 1.1 \pm 0.6 \text{ mb}$. The uncertainty was composed of the statistical uncertainty, $\sim 20\%$, and an estimated systematic uncertainty of $\sim 37\%$ (Table 5.1). The cross section is consistent with the cross section calculated with

FRESCO (0.7 mb) using optical potentials derived from fits to the angular distribution of the reaction $^{12}\text{C}(^{12}\text{C},^{11}\text{C})^{13}\text{C}$ at 50 MeV/nucleon [82].

5.2.3 Deuterated Polyethylene Target

The cross section for neutron transfer from deuterium in the deuterated polyethylene target is slightly more complicated. The first step is to determine the total number of incoming beam particles, n_b . The deuterated polyethylene target was only a $\sim 2 \times 2 \text{ cm}^2$ square which did not cover the whole beam profile, so corrections had to be applied to account for beam particles that missed the target. The percentage of incoming nuclei that would strike the deuterated polyethylene target was determined to be 90% by ST MoNA simulations. This, along with the data from the scalers, provides a total incoming particle number of $n_b = 2.36 \times 10^8$.

The second step is to calculate the number of deuterium atoms in the $t_{t,CD2} = 440 \text{ mg/cm}^2$ deuterated polyethylene target with a modified version of Eq. 5.5.

$$n_{t,\text{deuterium}} = \frac{N_H/N_C * F_D * N_A t_{t,CD2}}{M_C + N_H/N_C * (F_D M_D + F_H M_H)} \quad (5.8)$$

N_H/N_C is the ratio of hydrogen to carbon in the target, F_D is the fraction of the hydrogen that is deuterium, and F_H is the fraction of hydrogen that is ^1H . N_H/N_C , F_D , and F_H were determined using Rutherford Backscattering Spectrometry (RBS) analysis [83], with data taken at the Hope Ion Beam Analysis Laboratory. For a given angle the energy loss of the backscattered ion depends on the mass and charge of the target nuclei. This allows for a determination of the composition of the target material. Shown in Fig. 5.3 are RBS simulations for protons impinging upon a carbon (red line) and a CH_2 (black line) target.

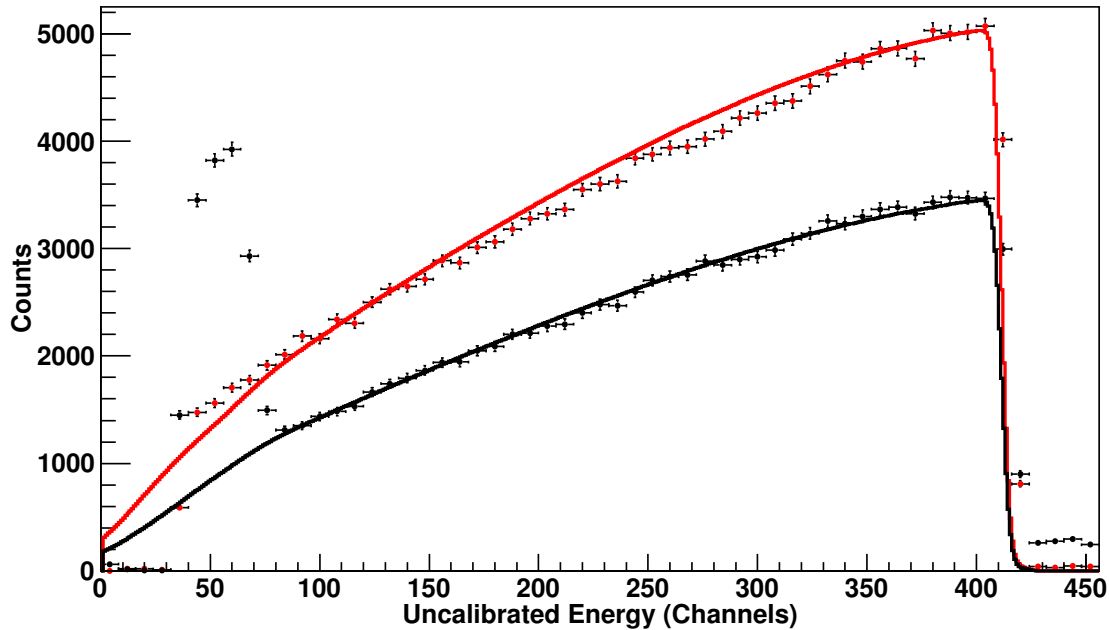


Figure 5.3: RBS simulations using 3.4 MeV protons impinging upon a carbon (red line) and a CH_2 (black line) target are compared to data from RBS analysis, also using 3.4 MeV protons. The carbon data (red points) and deuterated polyethylene data (black points) were normalized to the simulated carbon target. There is good agreement between the simulated deuterated polyethylene target and the data, which indicates that the ratio of carbon to hydrogen is 1:2.

It is compared to RBS data for a carbon and deuterated polyethylene target, normalized to the experimental carbon target data. The simulated CH_2 target matched the deuterated polyethylene target data, which indicates that the ratio of hydrogen to carbon is $N_H/N_C = 2$.

The peak centered at channel 60 in Fig 5.3 is from protons backscattering off of deuterium. The strength of the peak allows for determining the deuterium to hydrogen ratio. A visual inspection of the targeted showed some inhomogeneities, so the RBS analysis was repeated at 5 different locations across the target, as shown in Fig. 5.4. From the ratio of the low energy peak to the rise it is possible to determine the percentage of hydrogen that is deuterium. The purity of deuterium was 100%, 100%, 100%, 75%, and 50% for the five locations, respectively. To mitigate the non-uniformity of the deuterated polyethylene target, the average purity was

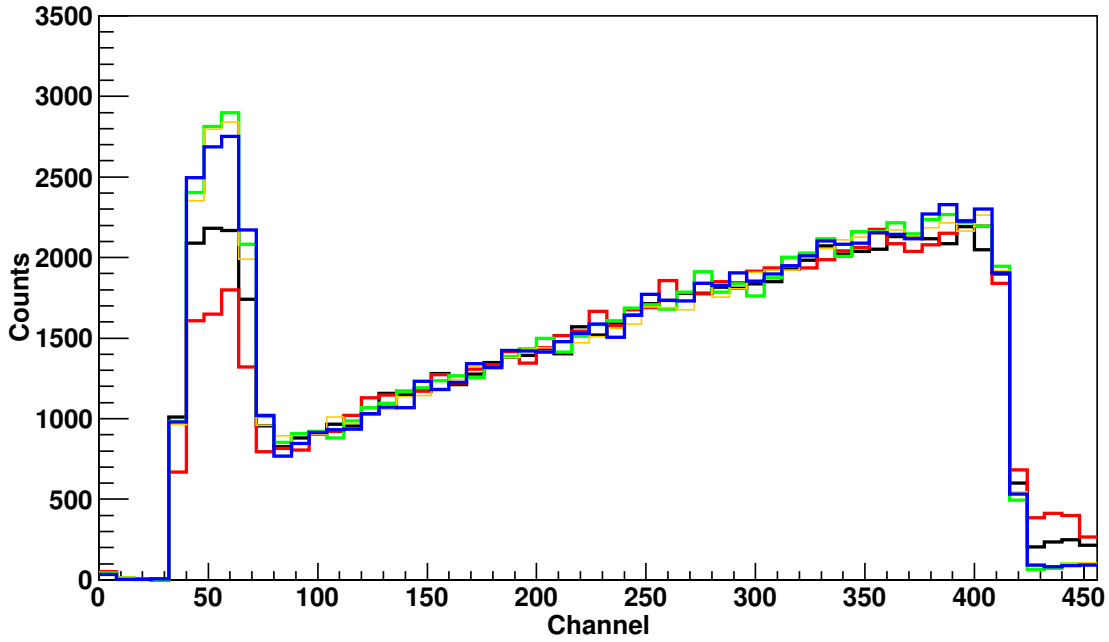


Figure 5.4: RBS data for five different locations on the deuterated polyethylene target, impinged with 3.4 MeV protons. Each data set was normalized so the total number of incoming protons were the same. The strength of the peak between channel 30 and 70 is indicative of the percentage of hydrogen in the target is deuterium.

used ($F_D = 0.85 \pm 0.15$). The total number of deuterium atoms in the deuterated polyethylene target was calculated to be:

$$n_{t,deuterium} = \frac{2 * 0.85 * N_A t_{t,CD2}}{M_C + 2 * (0.85 M_D + 0.15 M_H)} = (2.8 * 10^{22} \pm 0.4 * 10^{22}) / cm^2 \quad (5.9)$$

The final value necessary to calculate the cross section is the total number of reactions due to neutron transfer from deuterium. Using the number of reactions in the resonance (531), the efficiencies (ϵ_d , ϵ_a , and ϵ_{lt}), and Eq. 5.7 gives the total number of reactions as $n_{r,total} = 8650 \pm 300$. The expected number of transfers from carbon was calculated as:

$$n_{r,carbon} = \frac{n_b \sigma_{carbon} n_{t,carbon}}{10^{27}} = 4150 \pm 800 \quad (5.10)$$

where σ_{carbon} is the cross section measured in Section 5.2.2 and $n_{t,carbon}$ is the total number of carbon atoms in the target which is given by:

$$n_{t,carbon} = \frac{N_A t_{t,CD2}}{M_C + 2 * (0.85M_D + 0.15M_H)} = 1.65 * 10^{22} / cm^2 \quad (5.11)$$

Subtracting the number of reactions due to carbon from the total number of reactions gives the number of transfers from deuterium as $n_{r,deuterium} = 4500 \pm 1100$.

Table 5.2: The number of reaction events from different target nuclei for the CD2 target.

Total	Carbon	Deuterium
8650±300	4150±800	4500±1100

Finally, with these numbers and Eq. 5.4 the cross section for neutron transfer from deuterium calculated to be $\sigma_{deuterium} = 0.7 \pm 0.5$ mb. The systematic error is 50% for the deuterium transfer as listed in Table 5.1. The measured cross section is consistent with FRESKO calculations for the transfer from deuterium using several different global optical potentials [36, 37, 38]; which resulted in calculated cross sections from 1–2 mb.

Chapter 6

Summary and Outlook

6.1 Summary

The first observation of a neutron-unbound state in ^{15}Be has been measured using invariant mass spectroscopy. The neutron-unbound state was populated using neutron pick-up from a 440 mg/cm^2 deuterated polyethylene target with a 59 MeV/u ^{14}Be secondary beam. Neutrons from the decay of the unbound state in ^{15}Be were measured using MoNA whereas the charged fragments were deflected with the Sweeper magnet and detected in the focal plane box using a suite of charged particle detectors. Monte Carlo simulations which take into account acceptances, resolutions, and the interaction of the neutron within MoNA were compared to an invariant mass spectrum which was fitted using an energy-dependent Breit-Wigner distribution. The best fit to the data was achieved using $\ell = 2$ with the resonance energy of $1.8 \pm 0.1\text{ MeV}$ and a width of $575 \pm 200\text{ keV}$. The resonance was assigned to the predicted $5/2^+$ state. This removes the possibility that the $5/2^+$ state in ^{15}Be can serve as an intermediate decay for ^{16}Be , confirming the results from [13]. The cross section for neutron pick-up from carbon was measured to be $\sigma_{\text{carbon}} = 1.1 \pm 0.6\text{ mb}$, whereas the cross section for neutron pick-up from deuterium was measured to be $\sigma_{\text{deuterium}} = 0.7 \pm 0.5\text{ mb}$.

6.2 Outlook

The presented work does not solve the problem of whether the $3/2^+$ or the $5/2^+$ state is the ground state of ^{15}Be . In a previous work the lower limit of the $3/2^+$ state was determined to be 1.54 MeV [17]. This means that if the $3/2^+$ state is located between 1.54 and 1.8 MeV it will correspond to the ground state of ^{15}Be . To determine if the $3/2^+$ or the $5/2^+$ is the ground state of ^{15}Be it is necessary to determine the location of the $3/2^+$ state.

The best way to do this task is two proton stripping from ^{17}C which will primarily populate the $3/2^+$ of ^{15}Be and which was attempted in Ref. [17]. Once the $3/2^+$ state is populated it will primarily decay to the first excited state in ^{14}Be at 1.54 MeV and then decay by two neutron emission to ^{12}Be [21]. This decay path was suggested by the data of Ref. [17], however the statistics were not sufficient to reconstruct the 4-body decay energy. Three neutron decays require high statistics due to the cuts necessary to determine if the events are true three neutron events or if one or two of the neutrons interacted multiple times.

The second possibility is that the $3/2^+$ state will decay down to the ground state of ^{14}Be . This decay path was not observed in Ref. [17] and is expected to be small and thus will also require high beam rates to measure that pathway.

At the present time the intensities of the NSCL are not sufficient to determine the location of the $3/2^+$ state. However, with the expected beam intensity at the Facility for Rare Isotope Beams (FRIB) which is currently under construction, this question will be resolved. Currently the only facility that has the intensities to perform this experiment is the Radioactive Isotope Beam Factory (RIBF) at RIKEN. Another facility that will be able to deliver the necessary beam intensities for this experiment is the Facility for Antiproton

and Ion Research (FAIR) will have the intensities necessary once it comes online to perform this experiment.

APPENDIX

Appendix

Optical Model Potentials Parameters

The optical model potential parameters used in FRESKO to calculate the cross sections for neutron pick up from deuterium and carbon are listed in Table A.1, A.2, and A.3. The subscripts v , s , so , i denote the volume interaction, surface interaction, spin-orbit interaction, and the imaginary part of those interactions, respectively.

To perform the the calculation for neutron pick-up from deuterium FRESKO requires the potential between ^{14}Be and ^2H (Table A.1), ^{14}Be and ^1H , and ^{15}Be and ^1H (Table A.2).

Table A.1: Optical model potentials parameters used
to model the interaction between ^{14}Be and ^2H .

Ref.	V_v MeV	r_v fm	a_v fm	$V_{v,i}$ MeV	$r_{v,i}$ fm	$a_{v,i}$ fm	$V_{s,i}$ MeV	$r_{s,i}$ fm	$a_{s,i}$ fm	V_{so} MeV	r_{so} fm	a_{so} fm
Ref. [36]	55.9	1.18	0.72	0.00	0.00	0.00	29.1	1.27	0.82	6.0	0.87	0.87
Ref. [37]	42.0	1.17	0.81	16.7	1.56	0.81	0.00	0.00	0.00	3.7	1.23	0.81
Ref. [38]	66.9	1.15	0.75	7.90	1.35	0.61	7.50	1.40	0.68	3.6	0.97	1.01

Table A.2: Optical model potentials parameters used
to model the interaction between ^{14}Be and ^{15}Be with ^1H .

Reference	Isotope	V_v MeV	r_v fm	a_v fm	$V_{v,i}$ MeV	$r_{v,i}$ fm	$a_{v,i}$ fm	V_{so} MeV	r_{so} fm	a_{so} fm
Ref. [35]	^{14}Be	43.2	1.2	0.7	5.9	1.2	0.4	4.5	1.2	0.7
Ref. [35]	^{15}Be	43.8	1.2	0.7	5.9	1.2	0.4	4.5	1.2	0.7

To calculation the cross section for neutron pick-up from carbon, FRESKO requires the

potential between ^{14}Be and ^{12}C , ^{14}Be and ^{11}C , and ^{15}Be and ^{11}C . The best potential for each interaction came from a $^{12}\text{C}(^{12}\text{C},^{11}\text{C})^{13}\text{C}$ reaction and was used for all three interactions. The potential is given in Table A.3.

Table A.3: Optical model potentials parameters used to model the interaction between ^{14}Be and ^{12}C , ^{14}Be and ^{11}C , and ^{15}Be and ^{11}C .

Reference	V_v	r_v	a_v	$V_{v,i}$	$r_{v,i}$	$a_{v,i}$
	MeV	fm	fm	MeV	fm	fm
Ref. [82]	150	0.64	0.884	25.0	1.017	0.73

BIBLIOGRAPHY

BIBLIOGRAPHY

- [1] E. Rutherford *et al.*, Proceedings of the Royal Society A **123**, (1929).
- [2] N. Bohr and J. Wheeler, Phys. Rev. **56**, 426 (1939)
- [3] M. Goeppert–Mayer, Phys. Rev. **78**, 16 (1950).
- [4] M. Goeppert–Mayer, Phys. Rev. **78**, 22 (1950).
- [5] O. Haxel, J. H. Jensen, and H. Suess, Phys. Rev. **75**, 1766 (1949).
- [6] I. Tanihata *et al.*, Phys. Lett. B, **160**, 380 (1985).
- [7] I. Tanihata *et al.*, Phys. Rev. Lett. **55**, 2676 (1985).
- [8] Z. Kohley *et al.*, Phys. Rev. Lett. **110**, 152501 (2013)
- [9] C.R. Hoffman *et al.*, Phys. Lett. B **672**, 1 (2009).
- [10] D. Steppenbeck *et al.*, Nature **502**, 207 (2013).
- [11] A.A. Korshennikov *et al.*, Phys. Rev. Lett. **90**, 082501 (2003).
- [12] G. Christian *et al.*, Phys. Rev. Lett. **108**, 032501 (2012).
- [13] A. Spyrou *et al.*, Phys. Rev. Lett. **108**, 102501 (2012).
- [14] F.M. Marqués *et al.*, Phys. Rev. Lett. **109**, 239201 (2012).
- [15] A. Spyrou *et al.*, Phys. Rev. Lett. **109**, 239202 (2012).
- [16] B. Blank and M. Ploszajczak, Rep. Prog. Phys. **71**, 046301 (2008).
- [17] A. Spyrou *et al.*, Phys. Rev. C **84**, 044309 (2011).

- [18] N. A. F. M. Poppelier, L. D. Wood and P. W. M. Glaudemans, Phys. Lett. B **157**, 120 (1985).
- [19] B. A. Brown and W. D. M. Rae, NUSHELL (Michigan State University, East Lansing, 2007).
- [20] E.K. Warburton and B. A. Brown, Phys. Rev. C **46**, 923 (1992).
- [21] Y. Kondo *et al.*, Phys. Lett. B **690**, 245 (2010).
- [22] T. Al Kalanee *et al.*, Phys. Rev. C **88**, 034301 (2013).
- [23] S. Fortier *et al.*, AIP Conf. Proc. **912**, 3 (2007).
- [24] M.S. Golovkov *et al.*, Phys. Rev. C **76**, 021605 (2007).
- [25] S.M. Brown *et al.*, Phys. Rev. C **85**, 011302 (2012).
- [26] T. Sugimoto *et al.*, Phys. Lett. B **654**, 160 (2007).
- [27] J.D. Bowman *et al.*, Phys. Rev. C **9**, 836 (1974).
- [28] R.A. Kryger *et al.*, Phys. Rev. C **53**, 1971 (1996).
- [29] O.B. Tarasov and D. Bazin, Nucl. Instrum. Meth. B **266**, 19-20 (2008).
- [30] V. Maddalena *et al.*, Phys. Rev. C **63**, 024613 (2001).
- [31] E. Sauvan *et al.*, Phys. Rev. C **69**, 044603 (2004).
- [32] Z. Elekes *et al.*, Phys. Lett. B **614**, 174 (2005).
- [33] I.J. Thompson, Program Fresco, Comp. Phys. Commun. **7**, 167 (1988).
- [34] I.J. Thompson and F. Nunes. *Nuclear Reactions for Astrophysics*. New York: Cambridge University Press, (2009).
- [35] D.G. Madland, OECD/NEA Spec. Mtg. Nucleon-Nucleus Opt. Mod. to 200 MeV, Paris (1997) p.129.

- [36] J. Bojowald *et al.*, Phys. Rev. C **38**, 1153 (1988).
- [37] Y. Han, Y. Shi and Q. Shen, Phys. Rev. C **74**, 044615 (2006).
- [38] H. An and C. Cai, Phys. Rev. C **73**, 054605 (2006).
- [39] M.S. Curtin *et al.*, Phys. Rev. Lett. **56**, 34 (1986).
- [40] I. Tanihata, Nucl. Phys. A **553**, 361 (1993).
- [41] F. Marti *et al.*, AIP Conf. Proc. **600**, 64 (2001).
- [42] D. J. Morrissey *et al.*, Nucl. Instrum. Meth. B **204**, 90 (2003).
- [43] B. Luther *et al.*, Nucl. Instrum. Meth. A **505**, 33 (2003).
- [44] T. Baumann *et al.*, Nucl. Instrum. Meth. A **543**, 517 (2005).
- [45] M.D. Bird *et al.*, IEEE Transactions on Applied Superconductivity **15**, 1252 (2005).
- [46] Saint-Gobain Crystals. BC-400, BC-404, BC-408, BC-412, BC-416 premium plastic scintillators (2005).
- [47] N. Frank, *Spectroscopy of neutron unbound states in neutron rich oxygen isotopes*. Ph.D. Thesis, Michigan State University, East Lansing, Michigan (2006).
- [48] W.A. Peters, *Study of Neutron Unbound States Using the Modular Neutron Array (MoNA)*. PhD Thesis, Michigan State University, (2007).
- [49] D.E. Groom, N.V. Mohkov, and S. Striganov. Atomic Data and Nuclear Data Tables **76**, 2 (2001).
- [50] K. Nakamura *et al.*, J. Phys. G: Nucl. Part. Phys. **37**, 075021 (2010).
- [51] G. Christian, *Spectroscopy of Neutron-Unbound Flourine*. Ph.D. Thesis, Michigan State University, East Lansing, Michigan (2011).
- [52] Wave Metrics. IGOR PRO 5.0.1.0. 10200 SW Nimbus, G-7, Portland, OR, USA.

- [53] K. Makino and M. Berz, Nucl. Instrum. Meth. A **558**, 346 (2006).
- [54] N. Frank *et al.*, Nucl. Instrum. Meth. A **580**, 1478 (2007).
- [55] H. Scheit. *Simple track for mona*. Technical Report, NSCL, (2006).
- [56] A.M. Lane and R.G. Thomas, Rev. Mod. Phys. **30**, 257 (1958).
- [57] G. Breit and E. Wigner, Phys. Rev. **49**, 519 (1936).
- [58] A. Bohr and B. Mottelson, *Nuclear Structure Volume 1: Single-Particle Motion*. Singapore: World Scientific Publishing (1969).
- [59] S. Agostinelli *et al.*, Nucl. Instrum. Meth. A **506**, 250 (2003).
- [60] J. Allison *et al.*, IEEE Transaction on Nuclear Science **53**, 270 (2006).
- [61] J.B. Birks, Proc. Phys. Soc. A **64**, 874 (1951).
- [62] R.A. Cecil, B.D. Anderson, R. Madey, Nucl. Instrum. Meth. A **161**, 439 (1979).
- [63] S. Meigo, Nucl. Instrum. Meth. A **401**, 365 (1997).
- [64] I. Tilquin *et al.*, Nucl. Instrum. Meth. A **365**, 446 (1995).
- [65] R.C. Byrd, W.C. Sailor, Nucl. Instrum. Meth. A **274**, 494 (1989).
- [66] M.W. McNaughton *et al.*, Nucl. Instrum. Meth. A **116**, 25 (1974).
- [67] M.W. McNaughton *et al.*, Nucl. Instrum. Meth. A **129**, 241 (1975).
- [68] P. Rose (Ed.), ENDF/B-VI Summary Document, Report BNL-NCS-17541, National Nuclear Data Center, Brookhaven National Laboratory, (1991).
- [69] Evaluated Nuclear Data File (ENDF) <http://www.nndc.bnl.gov/exfor/endl00.jsp>, 2011.
- [70] Geant4 Physics Reference Manual. <http://geant4.web.cern.ch>, 2011.

- [71] A. Heikkinen, N. Stepanov, P. Wellisch, *Bertini intranuclear cascade implementation in Geant4*, Proc. Computing in High Energy and Nuclear Physics, vol. MOMT008, (2003).
- [72] Y. Watanabe *et al.*, AIP Conf. Proc. **769**, 326 (2005).
- [73] Japanese Evaluated Nuclear Data Library (JENDL).
/http://wwwndc.jaea.go.jp/jendl/jendl.html, (2011).
- [74] B. Roeder, *Development and Validation of Neutron Detection Simulations for EURISOL*, *EURISOL Design Study*, Report: 10-25-2008-006-In-beamvalidations.pdf, pp 31-44 (2008).
- [75] R.A. Cecil, B.D. Anderson, R. Madey, Nucl. Instrum. Meth. A **161**, 439 (1979).
- [76] A. Del Guerra, Nucl. Instrum. Meth. A **135**, 337 (1976).
- [77] A. Spyrou *et al.*, Phys. Lett. B **683**, 129 (2010).
- [78] ENDF/B-BII.1 FE-56
<http://t2.lanl.gov/nis/data/endl/endfvii.1-n-pdf/fe56.pdf>, (2013).
- [79] Z. Kohley *et al.*, Nucl. Instrum. Meth. A, **682**, 59 (2012).
- [80] G.F. Bertsch *et al.*, Phys. Rev. C **57**, 1366 (1998).
- [81] M. Wang *et al.*, Chin. Phys. C **36**, 1603 (2012)
- [82] J.S. Winfield *et al.*, Phys. Rev. C **39**, 1395 (1989).
- [83] H.R. Verma, *Atomic and Nuclear Analytical Methods: XRF, Mossbauer, XPS, NAA and Ion-Beam Spectroscopic Techniques*. New York: Springer-Verlag Berlin Heidelberg (2007).